



University of Crete
Physics Department

Bachelor Thesis
Spinthaki Sofia

ULTRAFAST LASER INDUCED
NANOSTRUCTURING OF THIN FILM METAL
SURFACES

Supervisor: Dr Stratakis Emmanuel
Ultrafast Laser Micro- and Nano- Processing Lab
Institute of Electronic Structure and Laser
Foundation for Research and Technology-Hellas

HERAKLION
OCTOBER 2021

Contents

1. Introduction	2
2. Theoretical Basis.....	5
2.1 LIPSS - Properties and Classification.....	5
2.2 Physical Mechanisms of LIPSS formation	6
3. Experimental Methods	9
3.1 Experimental Setup	9
3.2 Materials.....	12
3.3 Irradiation Methods	13
3.3.1 Static Irradiation	13
3.3.2 Dynamic Irradiation	13
3.4 Characterization Methods.....	15
3.5 Cell adhesion methods	18
3.5.1 Cell cultures	18
3.5.2 Immunocytochemical assay for confocal microscope observations	19
4. Results	20
4.1 Study of thin film compared to bulk materials.....	20
4.1.1 Comparative study of Ni films.....	20
4.1.1.1 Calculation of damage threshold fluence of Ni films.....	20
4.1.1.2 Parametric study of different thicknesses of Ni films.....	27
4.1.2 Comparative study of Cr films.....	38
4.1.2.1 Calculation of damage threshold fluence of Cr films.....	38
4.1.2.2 Parametric study of different thicknesses of Cr films.....	41
4.2 Fabrication of nanowires on Cr thin films	48
4.2.1 Nanowires area on 400 nm Cr film	48
4.2.2 Nanowires area on 250 nm Cr film	52
4.2.3 Nanoislands area on 250 nm Cr film	53
4.2.4 Cell adhesion on nanowires and nanoisland surfaces	54
5. Conclusion	56
Bibliography.....	57
Acknowledgements	58

1. Introduction

During the last two decades, the fields of nanotechnology and lasers are growing rapidly, introducing more and more innovative ideas and techniques, both in modern science and the industry. Specifically, materials nanostructuring has become a promising alternative for the modification of the functionalities of conducting and insulating, as well, materials. The manufacturing of nanostructured materials has provided a variety of applications in electronics, medicine, optics, etc., that have already been integrated in our daily life.

One appealing aspect of nanostructuring is the controllable surface modification induced by pulsed lasers. This technique was firstly discovered in 1965 by Milton Birnbaum ^[1], when he noticed some periodic structures that were created after the irradiation of a germanium wafer with multiple laser pulses. These self-organized periodic surface structures featured a period close to the wavelength of the laser and appeared in many sizes: from few tens of nm up to several μm . Nowadays, they are commonly referred to as Laser Induced Periodic Surface Structures (LIPSS).

LIPSS, also called ripples, are a universal phenomenon that can be observed on almost any material after its irradiation by short laser pulses, with durations in the picosecond to femtosecond range. They can be classified according to their spatial periods and the orientation to the linear laser beam polarization that is used for their generation. Low Spatial Frequency LIPSS (LSFL) have a period that is larger than half the laser wavelength (λ). Based on the formation mechanism, LSFL can either be oriented parallel or perpendicular to the laser beam polarization. On the other hand, High Spatial Frequency LIPSS (HSFL) feature a period that is smaller than half the laser wavelength.^[2] Another interesting characteristic of LIPSS, is the wide variety of morphologies in which they come in: grooves, spikes, nanowires, etc.

There are many theories that attempt to explain the physical mechanisms behind the formation of LIPSS on materials. All of them share one common notion: the surface of the material that is to be nanostructured needs to feature corrugation. One approach suggests that laser light gets scattered due to the surface's roughness and leads to its interference with the incident pulse. Another popular one discusses the surface plasmon coupling theory and how the coupled surface plasmons interfere with the laser beam during the irradiation. For both mechanisms, interference results in a spatial redistribution of the beam intensity, which is imprinted in the surface through many mechanisms: ablation, amorphization, and others.^[3]

The main reason for the uprising of LIPSS in the field of research and industry, is the simplicity and robustness of their manufacturing process. The evolution of industries in the modern world has led to the constant search of quicker, more economic and environmental-friendly techniques, avoiding the necessity of strict environmental conditions like clean rooms or high vaccum. Thus, the fact that the fabrication of nanostructures with complex surface functionalities can be conducted using an industrial short pulse laser, in ambient air, proves why they have gained more and more interest in the last years.

Moving on to the actual applications of the fabrication of LIPSS on a material's surface, the properties of LIPSS can be multiple: from optical and mechanical to chemical. A very unique idea that has risen in the past decade, is the imitation of biological surfaces. Natural evolution has contributed to the vast complexity of the animal species, for many thousands of years. For example, the nano-scale structure of the surface of a plant's leaf presents such a morphology that can provide the property of hydrophobicity or hydrophilicity^[4]. Another example is the wings of insects, which are nanostructured by nature in such a way that their sunlight reflectivity is minimal. All these exceptional properties can be given to materials, through the laser fabrication of their surfaces. This is called biomimetic laser engineering.

The topic of this diplomatic thesis is the fabrication of LIPSS, in the form of nanowires, in metal film surfaces, as well as the study of nanostructuring of thin metal films compared to bulk film metals. Therefore, the content of this thesis is split into two main sections: nanowires fabrication and comparative study of thin and bulk metal films.

During the last years, the morphology of nanowires has been studied in the literature more and more. The most important property of a nanowires' surface morphology is the special manipulation of light that it provides. Nanowires are subwavelength parallel metal ridges or wires, that can serve as a polarizing element due to the grating type metasurface that they form. Research literature of the last years, indicated that thin film metals can be structured to have a nanowires morphology, through femtosecond pulsed laser beams^[5]. This surface modification technique can be applied for the manufacturing of Wire Grid Polarizers, that can be used for the polarization of light that is in Mid-IR spectrum.

When it comes to the study of LIPSS on thin film metals compared to bulk materials, the modern literature lacks many information upon this topic. The interaction of light and material has been explored only in the regime of bulk materials. Experiments and studies show that the thinner the film of a material is, the more different the interaction between light and material is. Therefore, the physical mechanisms that are hidden behind this phenomenon, need to be explored in more depth.

In this work, we are going to discuss the experimental methods and results of the study of fabrication of nanowires in thin film metals, so that they can be used in the

manufacturing of Wire Grid Polarizers. Also, there will be a detailed display of the experiments' findings, concerning the comparative study of thin film metals. Lastly, we are going to present the conclusions of the most important data that were received, during this thesis.

2. Theoretical Basis

2.1 LIPSS - Properties and Classification

Laser Induced Periodic Surface Structures (LIPSS) are a periodic arrangement of lines, that represent a linear surface grating structure [2]. This type of nanostructures falls in the category of laser irradiated, self-organized structures that are specifically oriented and take place within the laser beam spatial limits [6].

LIPSS are usually classified either as ripples (nanometric parallel lines) or as grooves (micrometric parallel lines) or spikes (micrometric cone-like structures). Ripples are observed either as High Spatial Frequency LIPSS (HSFL, *Figure 1a*) or as Low Spatial Frequency LIPSS (LSFL, *Figure 1b*). HSFL feature periods, Λ , significantly smaller than the irradiation wavelength, λ , that is $\Lambda < \lambda/2$. On the other hand, LSFL have periods larger than half the wavelength, $\Lambda > \lambda/2$. Additionally, grooves (*Figure 1c*) constitute the intermediate state between ripples and spikes (*Figure 1d*).

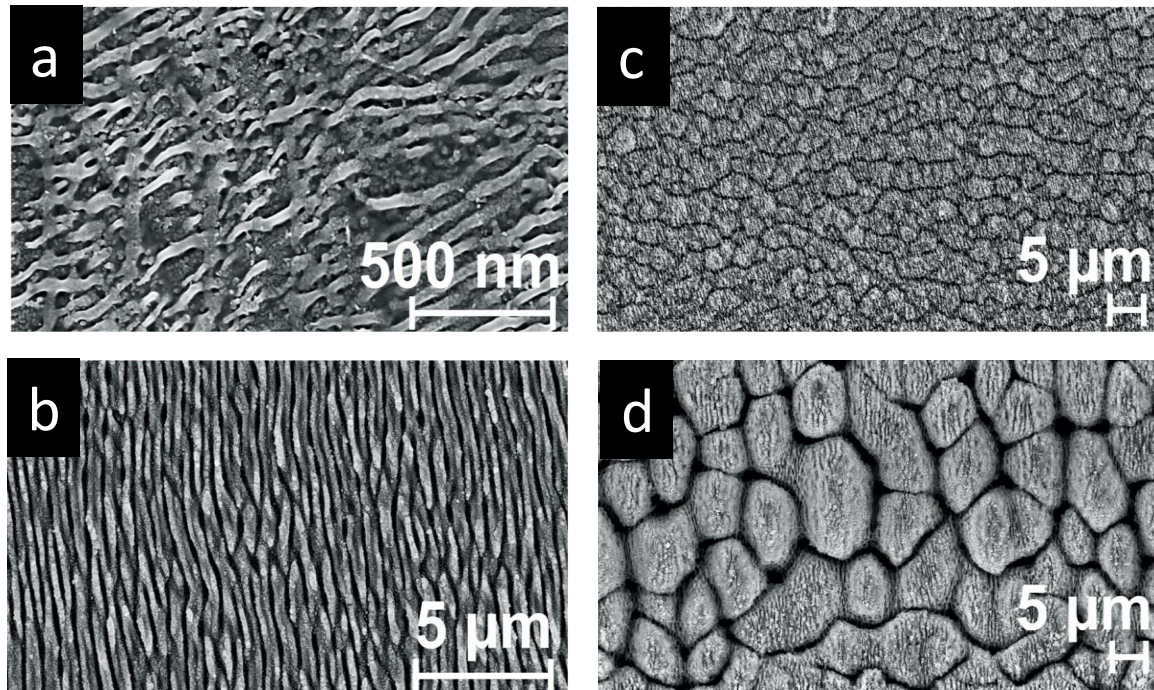


Figure 1

Reprinted from « *Laser engineering of biomimetic surfaces* », E. Stratakis, J. Bonse, J. Heitz, J. Siegel, G.D. Tsibidis, E. Skoulas, *Materials Science & Engineering, Article number: 141 (2019)* with permission from Elsevier^[4]

Top view of SEM images of LIPSS:

a. HSFL ripples, b. LSFL ripples, c. Grooves, d. Spikes

LSFL and HSFL show a very well-defined orientation, that is always determined with respect to the linear polarization state of the incident laser beam. In cases of more complex polarization states, circular, etc., it has been observed that they follow the orientation of the electric field of the laser beam.

For strongly absorbing materials, like metals or semiconductors, in most cases, LSFL are oriented perpendicular to the laser beam polarization, while HSFL are oriented parallel to the laser beam polarization.

For weakly absorbing materials, such as dielectrics, LSFL are mostly oriented parallel to the laser beam polarization, with periods close to λ/n , where n: the refractive index of the material. When it comes to the HSFL structures, they are observed in an orientation that is perpendicular to the polarization of the beam but, in some cases, also parallel.

2.2 Physical Mechanisms of LIPSS formation

LIPSS formation can be explained through various theoretical models, using a different approach each time. However, it is commonly known that the most important factor that contributes to the LIPSS formation, is the corrugation of the surface that is going to be irradiated.

Emmony et al. (1973) proposed that the laser beam that irradiates the surface, is scattered due to the surface roughness.^[7] They proposed a general surface scattering model that described the interference of the incident laser beam with the scattered waves. This model produces the following relation for the period of LIPSS:

$$\Lambda = \frac{\lambda}{1 \pm \sin\theta},$$

where:

λ : the laser wavelength

θ : the angle of the incident laser beam with respect to the perpendicular axis on the surface

The most well-established formation mechanism of LIPSS was introduced by Sipe et al. [8], [9], later on that same year. They considered that the energy deposition on a surface with an existing roughness, is not homogeneous. Furthermore, they claimed that the peak of the electromagnetic field, and thus the periodic patterns, depend not only on the angle of incidence but also on the polarization of the laser beam. In contrary to the theoretical

model of Emmony, this physical mechanism was based on the interference of the incident laser beam and the surface electron density waves, known as Surface Plasmon Polariton Waves (SPPs).

Specifically, when a high energy beam falls on the surface of a material, the energy deposition, at the irradiated region, is so intense that surface plasmons of the material get excited. A surface plasmon is the periodic wave that represents the spatial distribution of electric charge in the surface of a metal. These surface plasmons get coupled with the incident beam and lead to the occurrence of a new periodic wave distribution: the Surface Plasmon Polaritons (SPP). This way, the periodicity of the laser beam's wave length is transmitted to the periodicity of the wave of SPPs.

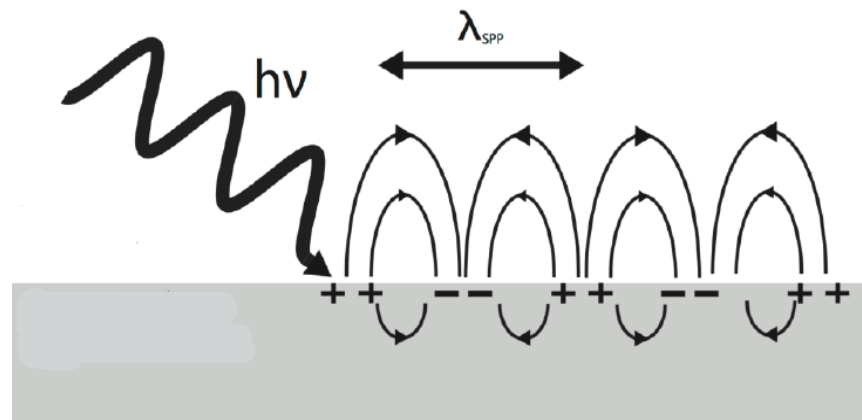


Figure 2

Reprinted from «Surface structuring of bulk and thin film materials with polarized ultrashort laser pulses», E. Skoulas, PhD^[6]

Image representation of the coupling of the incident beam and the Surface Plasmon Polariton Wave.

The laser beam energy that gets absorbed is distributed in the material through two main mechanisms: the energy-heat diffusion and the relaxation of the crystal lattice. The energy-heat diffusion refers to the distribution of the energy inside the material and therefore the following temperature increase. The mechanism of relaxation of the crystal lattice refers to the coupling between the SPP wave and the lattice of the crystal.

Specifically, after the irradiation of the material, the energy of the surface electron system (SPPs) decreases exponentially and leads to the transfer of the SPPs' periodicity to the crystal lattice. This periodic response of the lattice is what we call electron-phonon

relaxation. The time scale in which this phenomenon is observed, depends on the properties of each different material and it is called the relaxation time.

After the above procedures take place, the periodic distribution of the radiation's energy leads to the formation of periodic structures in the surface of the material. The periodicity of the structures is imprinted on the material's surface, through the periodic response of the crystal lattice during its relaxation.

The type of materials that can be fabricated with LIPSS are: metals and semiconductors. Metals are naturally consisted of a large number of charge carriers. That's why the concept of a plasmon wave is based on metal materials. However, semiconductors can show a metallic state when they are exposed in high temperatures, such as those of the irradiated surface. This way, a very large number of carriers gets excited in order to excite a surface plasmon wave.

Lastly, it must be noted that there are two main conditions for the formation of LIPSS on the surface of any material of the above. The first one is the existence of an interface. This condition refers to an interface between the material and a dielectric element, which, in most cases, is the air. Only this way can a surface plasmon get excited, during the material irradiation. Furthermore, the second condition refers to the corrugation of the material's surface. It is very important that the surface of the material is not smooth, as any imperfections of the surface, such as bumps and pits, provide an increased momentum of the incident beam. This is essential in order to excite a surface plasmon.

3. Experimental Methods

3.1 Experimental Setup

The experimental layout consists of four main parts: the laser source, the main optical path, the processing setup and the parameter measurement setup, as they are imaged in *Figure 3*.

The laser processing set up employed a variable repetition rate Yb: KGW Pharos- SP laser system (Light Conversion) with tunable pulse duration. The repetition rate ranges from single shot to 200 kHz and the central wavelength of the laser radiation is 1026 nm (Infrared-IR). The laser system provides the possibility of Second Harmonic Generation, as there is an option for the emission of a radiation with wavelength that is 513 nm (Visible-VIS). During the period of the experiments, the pulse width was selected to be 170 fs and the repetition rate was set to 1 kHz. Also, the laser beam that is emitted is linearly polarized.

The optical path is consisted of the optical elements that are placed and adjusted in such way that the emitted optical beam follows a very strict and narrow path which leads to the processing setup. The two beams of different wavelength follow different, but parallel to each other, optical paths. Each optical path is made up of optical elements, such as mirrors, beam splitters and polarizers, that are specifically selected accordingly to the type of radiation. Upon its emission, the laser beam is aligned through a mirror and a system of irises, that are placed in many different places of the path, in order to achieve alignment of high accuracy. A system of mirrors elevates and directs the beam into the processing setup, which was designed in such way that the beam falls perpendicularly to the sample.

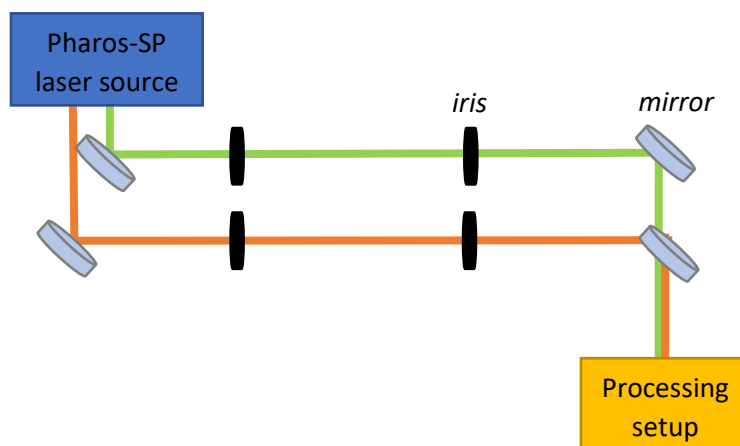


Figure 3

Top view of the main optical path of the experimental setup

The processing setup is depicted in *Figure 4*. Similar to the main optical path, the processing setup employs irises and mirrors that align and direct the beam to the sample stage. Additionally, power modulation of IR beam was achieved via an automatic rotating zero-order half wave plate that was placed behind a high extinction ratio (10000:1) glan-taylor linear polarizer. The power of the VIS beam was adjusted by a neutral density filter that provided a significant decrease of the beam power, when needed. The linear polarization of the beam was turned into circular, when needed, by a quarter-wave plate that was placed in front of a telescope system. A CCD camera was used for the in situ visualization of the sample processing, which emitted white light that passed through the dichroic mirror and depicted the surface of the sample while it was irradiated. In order to cut off the reflected radiation from the sample, a filter was put right above the sample stage. At last, a plano-convex lens of 200 mm focal length focused the beam on the sample stage. Each sample was mounted on top of a 3-axis motorized servo stage from Newport.

The parameter measurement setup refers to all the media used for the purpose of setting the experiment parameters and measuring the output parameters, such as the beam power in a certain point of the optical path. The movement of the sample stage as well as the laser parameters were controlled through a LabVIEW made program. The actual power of the laser beam was measured through a power meter that was put in the optical path, when needed.

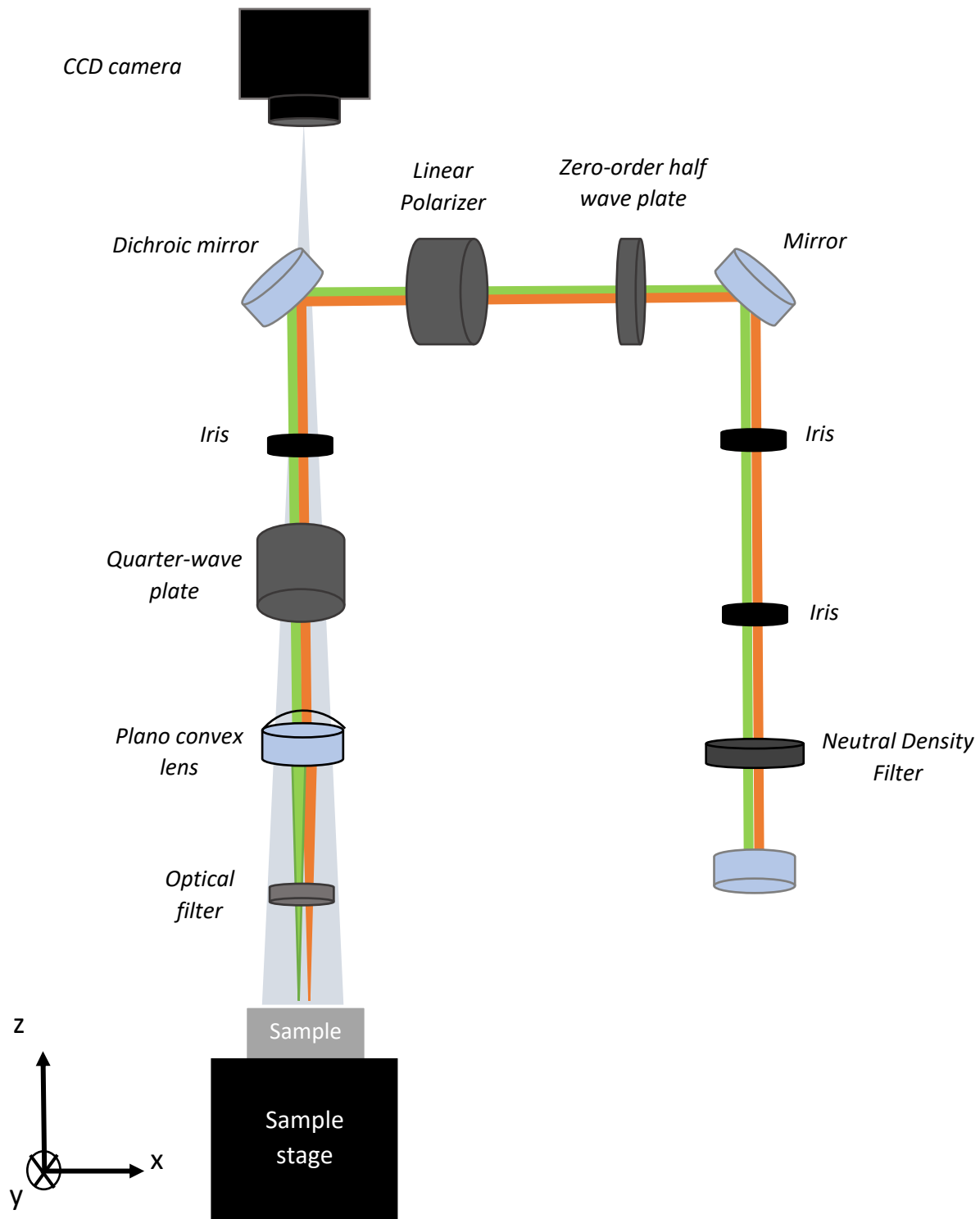


Figure 4
Side view of the processing setup

3.2 Materials

The materials, used as targets for irradiation with ultrashort laser pulses in this thesis, have a certain form: a metal film deposited on top of a dielectric substrate.

Usually, the substrate is fused silica (SiO_2 in amorphous form) as it has high working and melting temperature, and therefore it serves as the perfect substrate. Another type of dielectric substrate that is used is Aluminum Oxide (Al_2O_3), also known as Sapphire.

When it comes to the metal film, there are two different metals used for the purpose of this thesis: Chromium and Nickel. The main reason for the selection of such metals is the short relaxation time of their lattices, which means that the LIPSS that are formed on their surfaces are very well-defined, as the energy that gets transferred to the crystal lattice is high. Therefore, the use of noble metals, such as Au and Ag, was avoided due to their long relaxation time, which leads to the formation of LIPSS that are not discrete or even to no formation of LIPSS.

A detailed citation of all the samples, that were used in this thesis, based on their thickness and material, is presented in *Table 1*.

Thickness (nm)	Material
10	Cr on SiO_2
40	Cr on SiO_2
50	Ni on Cr Cr on SiO_2
100	Ni on Al_2O_3 Cr on SiO_2
250	Ni on SiO_2 Cr on SiO_2
400	Cr on Al_2O_3

Table 1

3.3 Irradiation Methods

3.3.1 Static Irradiation

For the purpose of fabrication of spots on the surface of the sample, the only laser parameters that needed to be adjusted, were: the repetition rate, the laser power and the burst packet. As it has been mentioned previously, the repetition rate has been kept constant throughout this whole thesis' experiments (1 kHz). The burst packet refers to the number of pulses that are emitted as the pulse picker is activated. Specifically, in this thesis the burst packet that was used for the creation of surface spots was 1 (single shot), in the context of the damage threshold calculation. The procedure followed for this purpose is discussed in detail, in the following chapter.

The burst packet was set to numbers larger than 1, for the definition of the focus point of the stage, regarding to the laser beam. More specifically, before working on a sample, it needed to be irradiated with tons of spots that differed in the Z axis position. Observation of these spots on the optical microscope, can easily lead to the realization of the Z position that corresponds to the focused point. The spot that was created at exactly the focused point, is smaller than all others and it also presents the larger percentage of damage-ablation in its center. This can be explained as the laser beam is gaussian which means that when the beam is focused, its waist line is minimum and its center power is maximum. Throughout the whole experimental studies, the focus on the Z axis is consistent and also checked upon many times.

3.3.2 Dynamic Irradiation

The laser processing of a material demands that the surface of the material gets irradiated in a consequent and dynamic way. This means that the incident laser beam falls for a certain amount of time on the surface of the sample while the sample moves on the 3 axes that the stage is allowed to move on. Therefore, the laser fabrication “print” is either a line or a surface on the sample.

A line is fabricated through the movement of the stage on one axis (either x or y) and the laser irradiation of the sample, at the same time. Except the laser fluence, the parameters that are essential for the creation of a line are:

- Scanning velocity (v): the speed at which the stage moves in each axis. This speed is directly related to the number of pulses that fall in the area of the laser spot size (Effective number of pulses), which is going to be examined further in the next part of the thesis. In the LabVIEW program, the scanning velocity in the x axis is the same as that in the y axis, while the scanning velocity in the z axis is different. The LabVIEW program was set to measure scanning velocity in millimeters per second (mm/s)
- Line length. It can be also set through the LabVIEW program. It is measured in micrometers (μm), as is every length parameter of LabVIEW.

The fabrication of a surface requires the definition of a slightly more extended set of parameters. Similarly, the parameters that are used in the laser fabrication of a surface are:

- Scanning velocity (v): same as the line parameter.
- Hatch (Y): the distance in between two consecutive lines of the surface. Each surface is created as a vertical set of many identical lines, where each line is deposited after the other, leaving a certain distance in the y axis. This distance is the so-called hatch. The hatch parameter is also related to the line overlap of the fabricated surface. As the hatch decreases, the line overlap increases, thus the effective number of pulses increases.
- Surface dimensions: the length and width of the surface which are selected through the LabVIEW program.

3.4 Characterization Methods

The laser fabricated structures of the irradiated samples were depicted and captured through an Optical Microscope and, mainly, a Scanning Electron Microscope (SEM) (JEOL JSM-7500F).

The Optical Microscopy was utilized in order to shape an approximate image of the general type and form of the LIPSS that were fabricated. This method provided the benefit of *in situ* visualization of the structures, as it did not require any preparation of the sample. However, this method was not sufficient in terms of image resolution and clarity, as the maximum magnification that could be achieved was 100x, that corresponded to a few hundreds of micrometers ($\mu\text{m}=10^{-6}\text{m}$).

On the other hand, SEM provided images with a resolution that reached even down to the nm (10^{-9} m) scale. Nevertheless, this imaging technique needs a certain sample preparation. Each sample that was to be examined in SEM, had to undergo a certain cleaning method before it was inserted in the SEM vacuum booth. The purity of the sample's surface ensured that the vacuum of SEM was at a high level as it is needed for its operation. This also provided a clear image of the sample. Specifically, each sample was immersed in a 75% ethanol dilution and into an ultrasonic cleaner. This way, every material residual that was ejected due to laser ablation, had been extracted, leaving the surface of the material completely clean.

It should be noted that SEM functions correctly when a sample is conductive. This is very important for the quality of the image as an insulating material would accumulate electron charge on its surface due to the incident electron beam. Therefore, the image would get blurry and would provide an unreliable source of data. For this reason, it was very important that there was no significant ablation of the conductive material of the samples, that is the metal film.

The images that were retrieved from SEM, were of high resolution (1280x1024) and the magnification of each image was determined according to the size of the periodic structures. A crucial factor, at this point, was that the LIPSS structures were depicted through SEM in such a way that their periodicity and topography was obvious and distinguishable. Moreover, this ensured the accuracy of their periodicity data, the analysis of which is described in the paragraphs below.

Each SEM image is analyzed through its transformation to a two-dimensional fast Fourier transform map. The program that is used for this purpose is *Gwyddion*, which transforms the imported image to a reverse space image via a 2D-FFT algorithm. The map that is generated is the spatial display of the intensity of the frequency in the reverse space. Essentially, each pixel of the FFT image corresponds to certain values of the frequency

space (measured in ($length^{-1}$)) while the intensity of the pixel corresponds to the intensity of the specific frequency. *Figure 5* depicts a SEM image of a LIPSS surface and its FFT image.

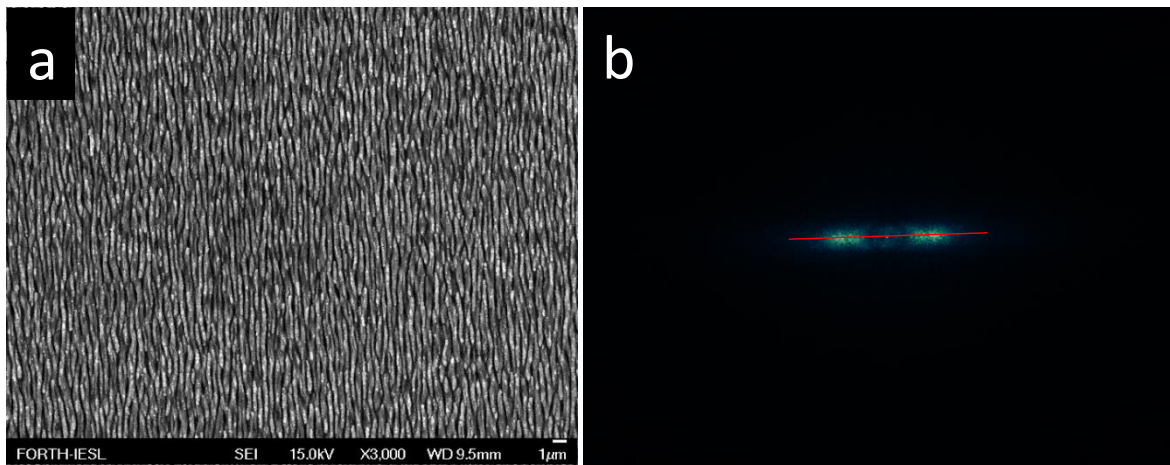


Figure 5

- a. SEM image of Cr surface, irradiated with ultrashort laser pulses
- b. FFT map of SEM image.

The profile of these frequencies along arbitrary lines, generates the diagram of the intensity as a function of spatial frequency. This diagram is consisted of vertical peak “lines” that can be fitted with great agreement through the Lorentz function. The fitting of Lorentz function then produces the parameters that are used for each peak. These parameters give the data that are used in the computation of the periodicity. The profile along the red line in *Figure 5b* corresponds to the intensity-frequency diagram in the *Figure 6*, where we can also see the Lorentz fit in the 1st peak.

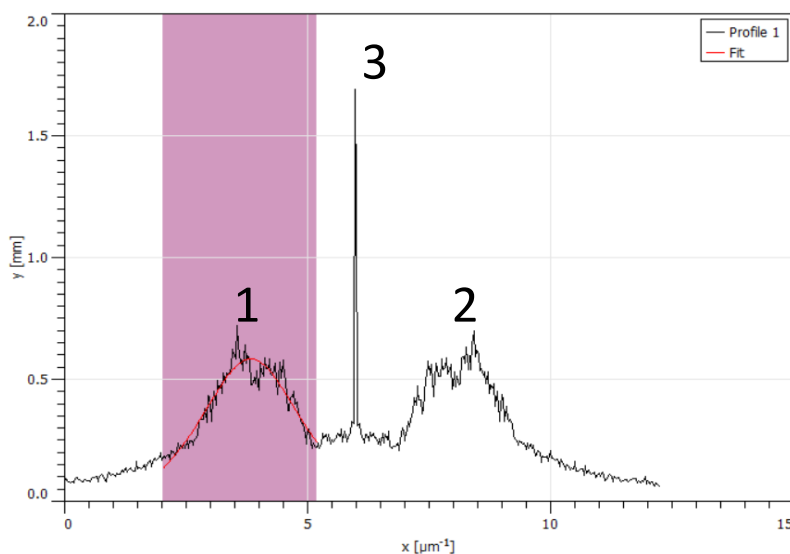


Figure 6

Lorentz fit of the peak of the intensity of frequency

Generally, the profile of the FFT image may consist of many peaks. However, when there is a distinguishable periodicity, there is always a set of lines (number 1 & 2 in *Figure 6*) that are positioned on both sides of a narrow central one (number 3). The central one corresponds to the frequency of zero, as it is always existing. The peaks that are selected, in order to obtain frequency data from them, are the ones that present the maximum intensity. This means that the corresponding frequency is also the most common one.

In order to calculate the periodicity Λ of the structures, we must first calculate the average frequency of peaks 1 and 2:

$$f = \frac{|f_2 - f_1|}{2},$$

where: f_1, f_2 are the frequencies corresponding to peak 1 and 2 accordingly.

Then, the periodicity is given by the equation below:

$$\Lambda = \frac{1}{f}$$

Taking into account that each frequency has an error that is also given by the Lorentz fit, we can calculate the error of the average frequency and then the error of the periodicity:

$$\delta f = \sqrt{\left(\frac{\partial f}{\partial f_1} \delta f_1\right)^2 + \left(\frac{\partial f}{\partial f_2} \delta f_2\right)^2} = \sqrt{\left(\frac{1}{2} \delta f_1\right)^2 + \left(\frac{1}{2} \delta f_2\right)^2} = \frac{1}{2} \sqrt{(\delta f_1)^2 + (\delta f_2)^2}$$

$$\delta \Lambda = \frac{d\Lambda}{df} \delta f = \frac{1}{f^2} \delta f$$

3.5 Cell adhesion methods

3.5.1 Cell cultures

In order to study the effect of different topographies of nanostructured samples on the adhesion, proliferation and orientation of live cells, a certain procedure of cell culture was conducted. For this study, NIH 3T3 mouse fibroblasts were used. NIH-3T3 cells are mouse embryonic fibroblasts derived from a cell line that was isolated and initiated at the New York University School of Medicine Department of Pathology in 1962. They were obtained from desegregated NIH Swiss mouse embryo fibroblasts by George Todaro and Howard Green. 3T3 stands for “3-day transfer, inoculum 3×10^5 cells” and is derived from the original cell transfer and inoculation protocol. This cell line has since become a standard fibroblast cell line and is usually used for DNA transfection studies [10].

The fibroblasts were grown in cell culture flasks using Dulbecco's modified Eagle's medium (DMEM) – High glucose (4500mg/L glucose) supplemented with 10% fetal bovine serum (FBS) and 1% penicillin/streptomycin solution (PS) at 37°C in a 5% CO₂ incubator, with medium renewal every 3 days. The samples were UV sterilized and transferred into sterile wells of 6-well plates. 80.000 cells/ml in culture medium were seeded on the samples for 1 and 3 days. Tissue culture plastic (TCP) coverslips were the control samples (reference material) in the experiments. *Table 2* summarizes the different time points and the specific experimental conditions per cell study.

Cell study on adhesion, proliferation, morphology and orientation of the Nanoislands and Nanowires of the Fused Silica coated with 250nm Cr	
NIH 3T3 fibroblasts (80000 cells/ml or per sample)	NIH 3T3 fibroblasts (80000 cells/ml or per sample)
Time point: 1 day (DIV)	Time point: 3 days (DIV)
Samples: Fused Silica coated with 250nm Cr and laser patterned in Nanowires and Nanoislands	Samples: Fused Silica coated with 250nm Cr and laser patterned in Nanowires and Nanoislands
Main objective: To investigate the effect of these topographies on cell adhesion, proliferation and orientation	Main objective: To investigate the effect of these topographies on cell adhesion, proliferation and orientation
ImmunoStaining procedure for observation under Confocal Microscope: DAPI for cell nucleus (cell proliferation), Actin Phalloidin @568nm for cytoskeleton (cell morphology and orientation) and Vinculin @ 488nm for cell adhesion	ImmunoStaining procedure for observation under Confocal Microscope: DAPI for cell nucleus (cell proliferation), Actin Phalloidin @568nm for cytoskeleton (cell morphology and orientation) and Vinculin @ 488nm for cell adhesion

Table 2

All the specific experimental conditions per cell study are listed.

3.5.2 Immunocytochemical assay for confocal microscope observations

For this assay, the medium was removed from samples and they were washed twice with Phosphate Buffered Saline (PBS) 1x (pH = 7.4) for 5 min and then fixed with 4% paraformaldehyde (PFA) for 15 min at RT. After removal of PFA solution, the samples were washed again twice with PBS 1x and treated with Triton-X100 0,1% solution in PBS for 5 min in order to permeabilize cell membranes. Then, the samples were washed twice with PBS 1x for 5 min and blocked using 2% Bovine Serum Albumin (BSA) in PBS solution for 30 min. Subsequently, the cells incubated with the first antibody overnight at 4oC. Next day, the cultured cells were washed twice with PBS 1x and incubated with the secondary antibody and actin phalloidin 568 (1:500) for 2 h and then a nuclear staining was carried out by 4,6-diamidino- 2-phenylindole (DAPI 1:10.000 in PBS) at RT. The first and second antibodies used in the present study are summarized in *Table 3*. Both 1st and 2nd antibodies were diluted in 1% BSA in PBS 1x solution, at the respective concentrations. The samples were transferred on microscope slides for observation using a ‘Leica SP8’ laser scanning confocal microscope.

First Antibody	Second Antibody	Phalloidins
Vinculin (mouse) (1:300)	Anti-mouse 488 (1:600)	Actin Phalloidin 568 (1:500)

Table 3
The first and second antibodies used for the various cell studies.

The cell number was determined by counting cell nuclei stained with DAPI. Nuclei number was assessed with ImageJ (cell counter plugin) ($n = 5$ field-of-view images for each topography/flat area/control and time point).

4. Results

The experiments of this thesis aimed in two main purposes: (1) the study of thin film materials compared to bulk materials and (2) the fabrication of nanowires in thin film materials. Therefore, the experimental results are going to be presented in two different parts.

Before moving on to the presentation of the experimental results, there are some basic parameters that need to be noted. During these experiments, the laser beam's repetition rate was set to 1 kHz at all time and the polarization of the beam was always linear. The only exception upon which the laser beam's polarization was not linear, is the study of fabrication of nanowires on Cr film samples, where it will be discussed further.

4.1 Study of thin film compared to bulk materials

In this part of the thesis, both of the metal materials, that were mentioned, are being studied: Chromium (Cr) and Nickel (Ni). The chromium samples that were utilized were of four different thicknesses: 10, 40, 100, 250 nm. The nickel samples were of three different thicknesses: 50, 100, 250 nm.

In order to explore the different LIPSS properties of thin film and bulk materials, there needed to be two different types of study. The first one was a parametric study that was conducted through the irradiation of all the different films, of the same metal, using the exact same parameters in each one of them. Secondly, another approach of studying thin films compared to bulk materials, was the experimental calculation of the damage threshold fluence of the thin film and bulk metals. Following, these two types of studies are going to be presented for each metal separately.

4.1.1 Comparative study of Ni films

4.1.1.1 Calculation of damage threshold fluence of Ni films

The damage threshold fluence is defined as the minimum laser energy fluence of a single laser pulse that causes any surface modification on a material, known as "damage". Knowing this threshold value is very important in the field of laser fabrication and

manufacturing as it sets the energy limit above which the material is not “transparent” to the laser radiation.

The dielectric materials (Al_2O_3 or SiO_2), used in the samples of this thesis, have a much higher damage threshold energy fluence than the metal films (Ni or Cr). Therefore, the laser radiation that falls on the samples leaves unharmed the surface of the dielectric substrate, for the whole range of energy fluences used in all the experiments of the thesis.

This study’s main purpose is the experimental definition of thin films’ damage threshold energy fluence, compared to bulk films. It was conducted for both 1026 nm and 513 nm radiation.

The experimental calculation of the damage threshold fluence that was carried out, in this thesis, is based on Liu’s work^[11], with slight changes. Liu’s paper is written based on his observations on irradiation of silicon surfaces with single and multi-shots. Specifically, Liu takes into consideration the inner and outer radius of the amorphous rings that form in a spot, due to the laser irradiation.

The spots are fabricated using a variety of different laser fluences. As it’s expected, the spots radius increases as the laser fluence increases. He considers that the growth of the outer (r_a) and inner (r_c) radii of the amorphous rings is consistent with the Gaussian-beam profile:

$$\begin{aligned} E(r_a) &= E_0 e^{-\frac{2r_a^2}{w_0^2}} = E_a \\ E(r_c) &= E_0 e^{-\frac{2r_c^2}{w_0^2}} = E_c \end{aligned} \quad (\text{I})$$

Solving the equations above, so that the dependence of each ring’s radius on E_0 is clear, we can see the linear relation between $r_{a,c}^2$ and $\ln(E_0)$:

$$\begin{aligned} r_a^2 &= \frac{w_0^2}{2} (\ln(E_0) - \ln(E_a)) \\ r_c^2 &= \frac{w_0^2}{2} (\ln(E_0) - \ln(E_c)) \end{aligned} \quad (\text{II})$$

Thus, the measurements of the inner and outer radii of the spots as well as the corresponding laser power, can lead to the calculation of $E_{a,c}$ and w_0 through the linear fit of the $r_{a,c}^2 - \ln(E_0)$ graph.

In this thesis, the actual technique that was followed in order to estimate the damage threshold fluence of any sample, slightly differs due to the different morphology of the spots that were formed. Using both IR and visible radiation, the fabricated spots appeared either as uniform “circles” and “ellipsoids” or as inner and outer rings (*Figure 7*).

Furthermore, the laser pulses that irradiate the samples are single shot. The energy range for the pulse irradiation of each sample was selected according to the images that were gotten *in situ* from the optical microscope of the lab. The maximum laser power was selected to be approximately 10 mW above the laser power that corresponds to the last visible spot, in the optical microscope. Then, the laser power dropped in an even smaller step from the maximum value to the power of the last visible spot and even lower, in order to create a very accurate plot of data.

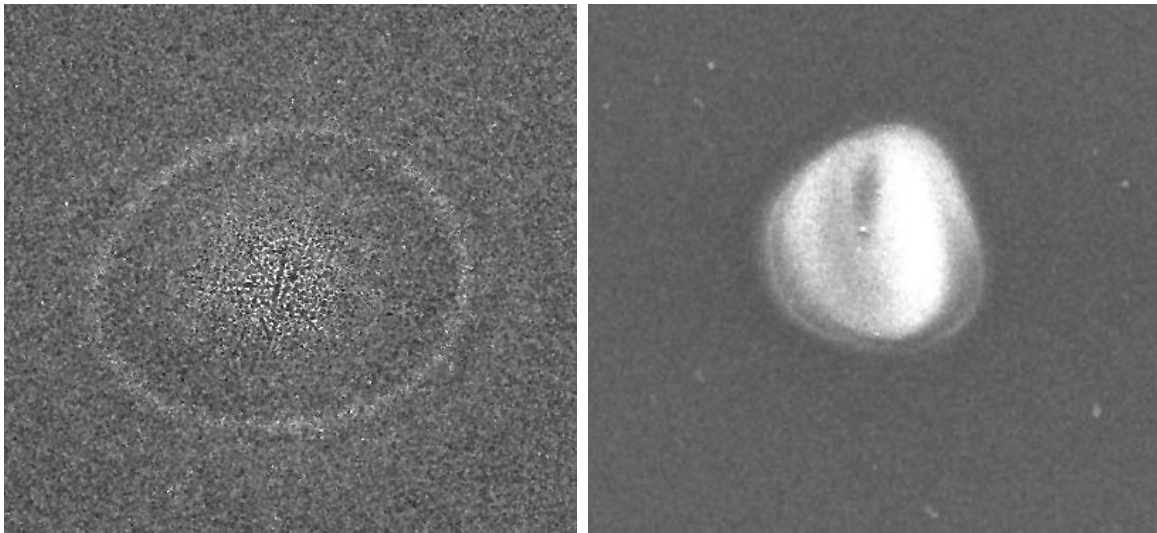


Figure 7

SEM images of irradiated spots with different shapes. The left spot is consisted of an inner and outer radius while the right spot is a uniform “circle”.

For this reason, the measurements were taken from the horizontal (r_b) and vertical (r_a) radius of the inner ring (when there is an outer ring). The measurement of the radius in two different axes serves for the spots that diverge from the circular shape, therefore leading to more accurate data.

Similarly with Liu’s technique, we take into consideration the equations (I), (II) only with the change of inner and outer radii (r_a and r_c) to vertical and horizontal radii (r_a and r_b):

$$r_a^2 = \frac{w_0^2}{2} (\ln(E_0) - \ln(E_a)) = s_a \ln(E_0) - t_a \quad (III)$$

$$r_b^2 = \frac{w_0^2}{2} (\ln(E_0) - \ln(E_b)) = s_b \ln(E_0) - t_b$$

Therefore, the linear relations from above, give the following equations of slope and intercept:

$$slope = s_a = s_b = \frac{w_0^2}{2}$$

$$intercept = t_a = t_b = -\frac{w_0^2}{2} \ln (E_{a,b})$$

The actual radii of the irradiated spots are measured through the *ImageJ* program. Each spot's irradiation was repeated three times in order to properly calculate the mean value of the radii and to minimize the measurement's error. Plotting both the values of r_a^2 and r_b^2 as functions of $\ln(E_0)$, the linear fit estimates the slope and intercept from the plot data. *Figure 8* shows how well the plot data fit into the linear form. The slope values that are extracted from the linear fittings of $r_a^2 - \ln(E_0)$ and $r_b^2 - \ln(E_0)$, are used for the calculation of the average slope (s) and its standard deviation (δs).

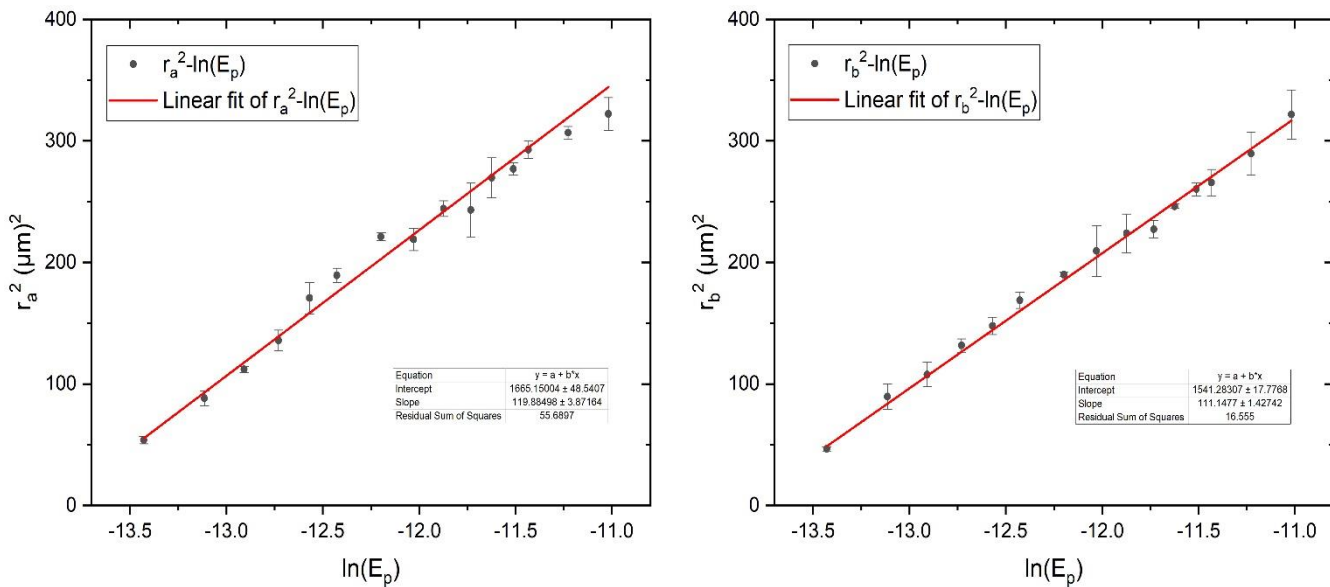


Figure 8

Example of plots of $r_a^2 - \ln(E_0)$ and $r_b^2 - \ln(E_0)$ that are linearly fitted.
The data are derived from spots that are fabricated in 250 nm Ni, using 513 nm radiation.

Therefore, the spot size of the beam and its error are given by:

$$w_0 = \sqrt{2s}$$

$$\delta w_0 = \frac{\sqrt{2}}{2\sqrt{s}} \delta s$$

Then, we use the value of the spot size in the calculation of the damage threshold energy:

$$E_{a,b} = E_0 e^{-\frac{2r_{a,b}^2}{w_0^2}} = E_0 e^{-\frac{r_{a,b}^2}{s}}$$

$$\delta E_{a,b} = \sqrt{\left(\frac{r_{a,b}^2}{s^2} E_{a,b} \delta s\right)^2 + \left(-\frac{2r_{a,b}}{s} E_{a,b} \delta r_{a,b}\right)^2},$$

where:

E_0 : the energy of the laser pulse that creates the smaller spot (that is visible),

$r_{a,b}$: the vertical and horizontal radius of this spot.

Finally, the damage threshold energy fluence is estimated through the following relations:

$$\Phi_{th} = \frac{2E_{a,b}}{\pi w_0^2} = \frac{E_{a,b}}{\pi s}$$

$$\delta \Phi_{th} = \sqrt{\left(\frac{2}{\pi w_0^2} \delta E_{a,b}\right)^2 + \left(\frac{E_{a,b}}{\pi s^2} \delta s\right)^2}$$

- $\lambda=1026\text{ nm}$

The implementation of the above procedure, in the data obtained from the spots that were fabricated using the 1026 nm beam, on all the Ni film samples, provides the following results:

Ni film thickness (nm)	Damage threshold fluence Φ (J/cm ²)	$\delta\Phi$ (J/cm ²)	Spot size w_0 (μm)	δw_0 (μm)
50	0.299	0.004	27.514	0.781
100	0.393	0.008	27.535	1.173
250	0.434	0.012	30.381	1.662

Table 3

Regarding the spot size of the IR beam, the mean value and the standard deviation give the following values:

$$w_{0,IR} = (28.477 \pm 1.347) \mu\text{m}$$

- $\lambda=513\text{ nm}$

Similarly, the data obtained from the spots that were fabricated using the 513 nm beam, on all the Ni film samples, are given in *Table 4*:

Ni film thickness (nm)	Damage threshold fluence Φ (J/cm ²)	$\delta\Phi$ (J/cm ²)	Spot size w_0 (μm)	δw_0 (μm)
50	0.057	0.005	8.426	1.365
100	0.203	0.005	15.444	0.809
250	0.263	0.002	15.200	0.287

Table 4

The average value of the spot size of the 513 nm beam (visible radiation) is:

$$w_{0,VIS} = (13.023 \pm 3.252) \mu m$$

Overall, the two studies of damage threshold fluence calculation, using 513 and 1026 nm beam, can be assessed through the following graph (*Figure 9*).

As we can see in the graph below, the experimental values of the damage threshold fluence show the same increasing trend as the theoretical curve that is represented through the continuous line. Also, the experimental values approach a plateau value, approximately at the value of 0.45 J/cm², which is also anticipated according to the theoretical data. However, there is a slight divergence of the actual experimental values compared to the theoretical one, which can be justified as theory does not always agree with the experimental data with great precision.

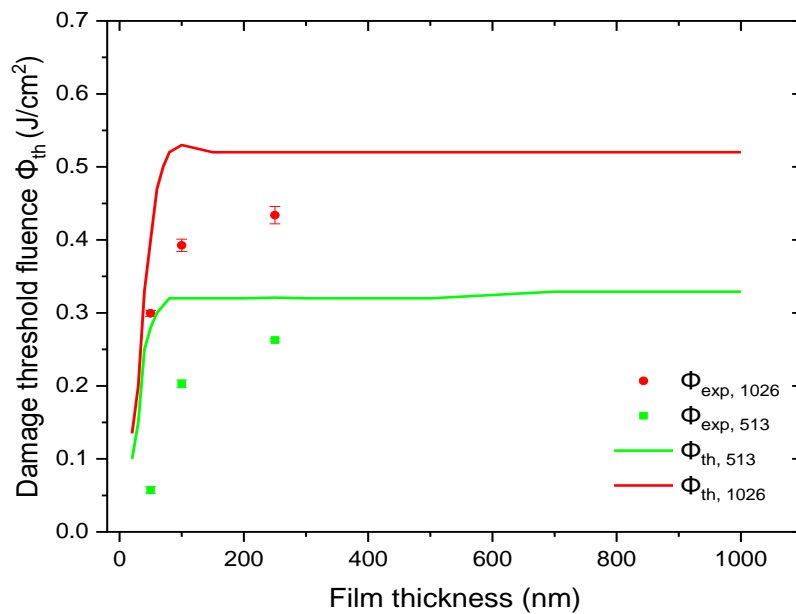


Figure 9

Graph of the experimental and theoretical values of damage threshold fluence as a function of the Ni film thickness.

4.1.1.2 Parametric study of different thicknesses of Ni films

This study was conducted using two different radiations: IR ($\lambda=1026$ nm) and VIS ($\lambda=513$ nm). The fabrication of structures was succeeded via the irradiation of the sample in lines. Therefore, there were three basic parameters that needed to be specified at the start of each experiment: the power range, the scanning velocity range and the length of the lines. Generally, all the fabricated lines had a length of 100 μm .

- $\lambda=1026$ nm

The power range that was selected in order to effectively compare the fabricated structures of 50, 100 & 250 nm Ni films was: 3.0 - 4.0 mW. The minimum step of power was: 0.2 mW, therefore leading to six different sets of power. The scanning velocity was set to vary from 0.1 to 1.0 mm/s, with a step of 0.1 mm/s, which corresponds to a total number of ten different values of velocity. In other words, for a specific value of power, a total amount of ten different lines was created, that correspond to the ten different values of scanning velocity.

As it has been mentioned before, the energy power that is measured during the experiment, is used for the calculation of the energy fluence of the laser beam. The equation that calculates the laser beam's energy fluence is expressed below:

$$\Phi = \frac{2E}{\pi w_0^2} = \frac{2P}{f \cdot \pi w_0^2},$$

where P: the laser power

f: the repetition rate of the laser (1 kHz)

w_0 : the spot size of the laser beam

Using the estimated value of the spot size of the IR beam from the damage threshold study ($w_0 = 28.5 \mu\text{m}$), the laser fluence is estimated to range from:

$$0.235 \text{ to } 0.314 \frac{\text{J}}{\text{cm}^2}$$

Similarly, the scanning velocity is related to the effective number of pulses in the area of a spot size. The relation that gives the value of effective number of pulses, for line scanning, is:

$$N_{eff, line} = \frac{2w_0 f}{v},$$

where v : the scanning speed.

Therefore, the range of the effective number of pulses, in this experiment, is:

57 to 570

Each different thickness was irradiated with a total of 60 lines. After the irradiation with the IR beam in the parameters that were mentioned above, the SEM images of these lines, indicated a significant difference in the fabricated structures of each thickness.

More specifically, the 250 nm Ni on SiO_2 sample exhibited a large number of lines that were ablated, in conditions of high effective number of pulses. However, the lines that were irradiated with a low effective number of pulses, were consisted of LSFL structures. *Figure 10* shows how the morphology of structures on 250 nm Ni sample changes according to the effective number of pulses.

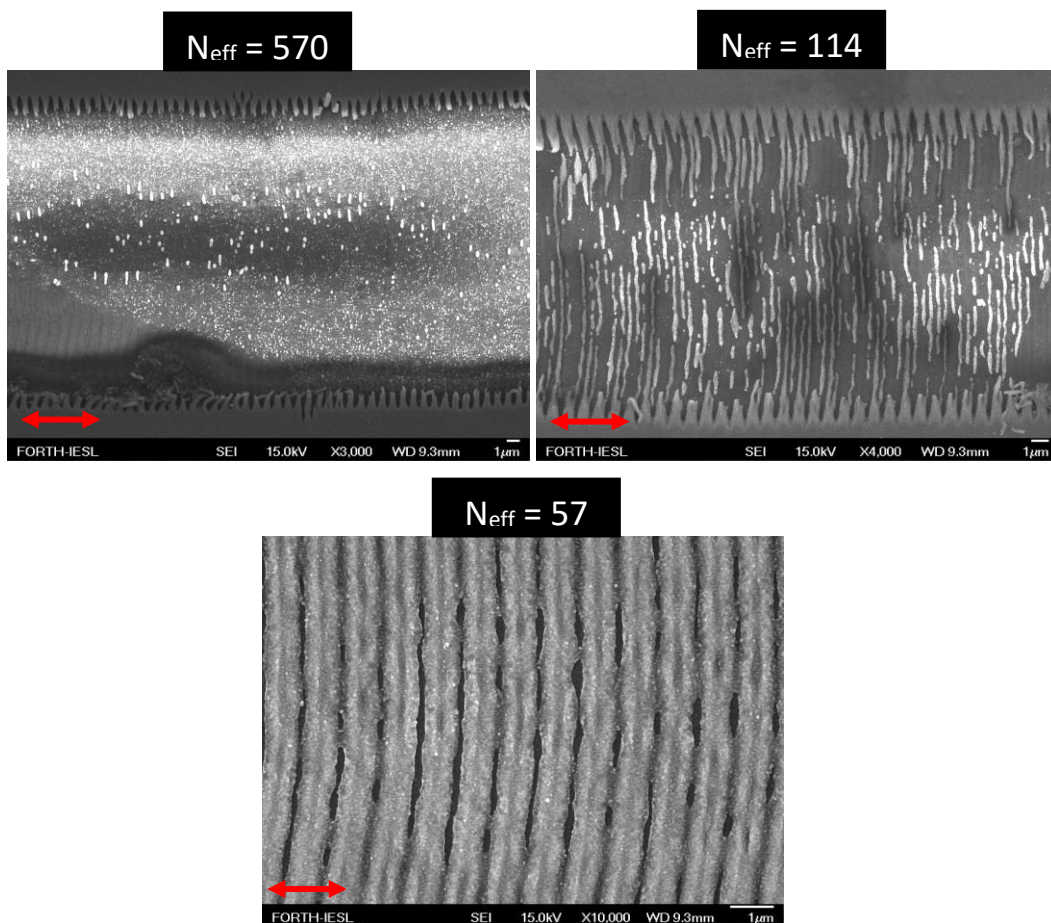


Figure 10
Images from SEM of 250 nm Ni sample.

All the lines were created using the same laser energy fluence (0.282 J/cm^2) while the effective number of pulses changes as it is shown. The red arrow symbolizes the direction of the polarization of the laser beam.

The LSFL structures of the 250 nm Ni sample resemble the morphology of nanowires. However, these nanowires are not very well oriented and their width fluctuates a lot among different conditions of number of pulses.

In the thinner films of Ni, all of the lines were fabricated, creating structures that were mainly HSFL in the 50 nm Ni sample, and LSFL in the 100 nm Ni sample. For large fluences, the fabricated lines were ablated in the center, where the intensity of the beam is at its maximum. This was mostly observed in the sample of 100 nm Ni, compared to the sample of thin film that is 50 nm Ni. Images from SEM, that represent the morphology of the structures in the 50 & 100 nm Ni samples, are depicted in *Figure 11*.

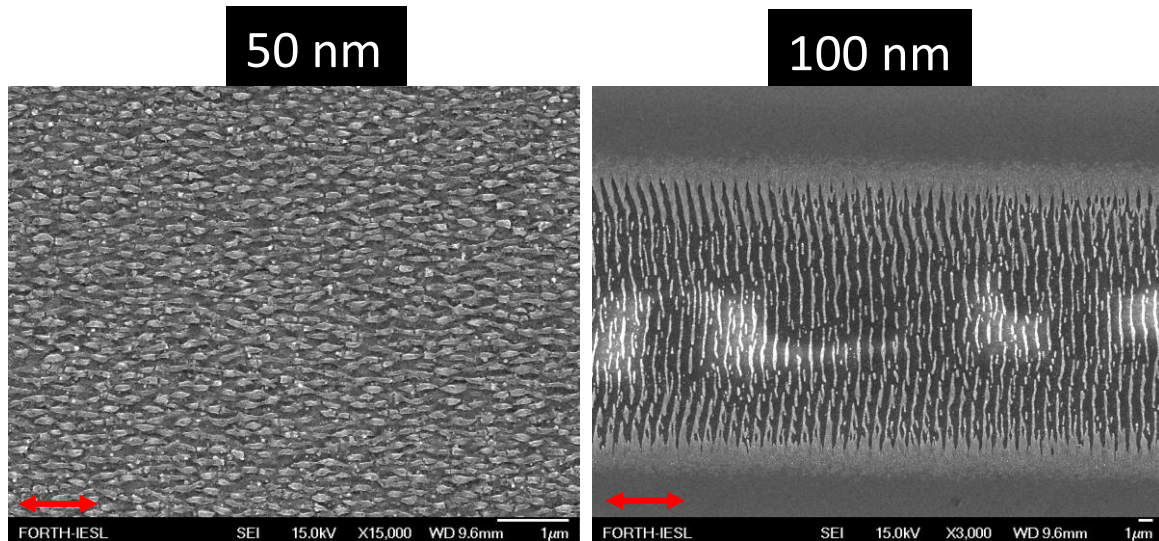


Figure 11

Images from SEM of 50 nm & 100 nm Ni sample.

All the lines were created using the same laser energy fluence (0.266 J/cm^2) and effective number of pulses (190).

As we can see in the images above, the periodicity of the structures differs both in direction and magnitude, in the two different thicknesses. The HSFL structures in 50 nm Ni have a very low periodicity ($\Lambda=182 \text{ nm}$) that extends in the axis that is parallel to the polarization of the beam. On the other hand, the 100 nm Ni sample appears to have LSFL structures that are oriented perpendicular to the laser polarization. Their periodicity is quite large ($\Lambda=840 \text{ nm}$) and their morphology also resembles nanowires that, however, don't maintain their shape, as they are broken in many parts. In *Figure 11*, the right image, that corresponds to the sample of 100 nm Ni, shows some white regions. These regions

are caused because of the ablation of the metal there, which exposes the dielectric substrate to the electron beam while taking the pictures with SEM.

An interesting set of structures that was fabricated in the 50 nm Ni sample is a “hybrid” of LSFL and HSFL structures (*Figure 12*). The specific parameters, that are written in *Figure 12*, create such conditions that there is a separation of the metal structures in LSFL and HSFL, simultaneously in the same line. In *Figure 12a*, there is an actual breakdown of the metal film into thin nanowires, perpendicular to the laser polarization ($\Lambda=664$ nm). Along with this morphology, we can see a second very different type that is HSFL structures oriented parallel to the laser polarization ($\Lambda=194$ nm). Furthermore, *Figure 12b* is consisted of structures that are mainly oriented parallel to the laser polarization ($\Lambda=209$ nm) while there is also a discrete periodicity in the axis perpendicular to the laser polarization ($\Lambda=1010$ nm).

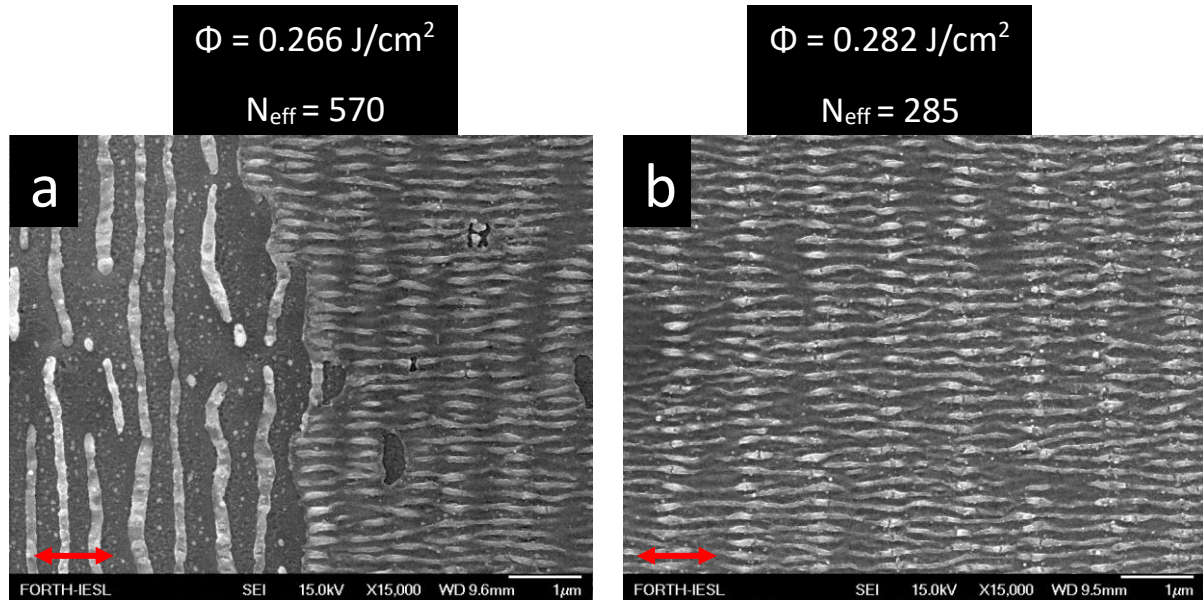


Figure 12
 Images from SEM of 50 nm Ni sample. Both topologies are consisted of LSFL and HSFL

In order to get an overall image of the dependence of the structures’ periodicities on laser energy fluence and the effective number of fluence, we need to construct the corresponding graphs. More specifically, each type of structure: LSFL or HSFL is categorized according to the energy fluence and the effective number of pulses that was used during its fabrication. Therefore, there are two main types of graphs that are needed for this purpose: periodicity as a function of fluence (while effective number of pulses is kept constant) and periodicity as a function of the effective number of pulses (while energy fluence is kept constant). These graphs are given below:

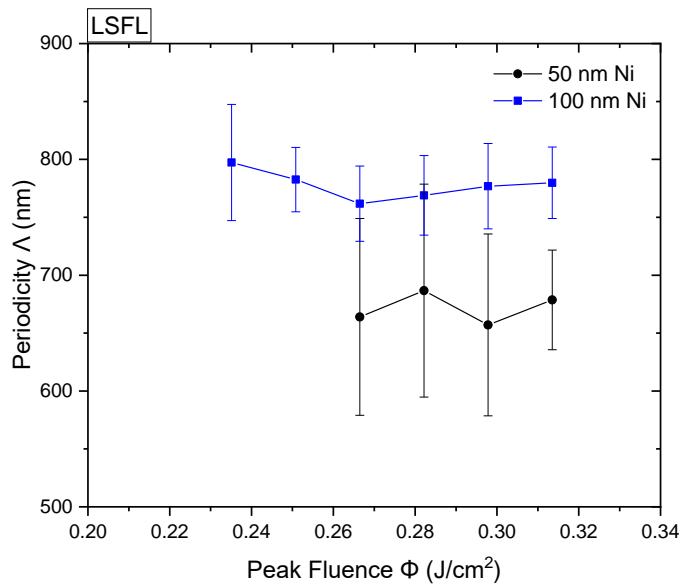


Figure 13
Graphs of periodicity as a function of laser fluence for $N_{eff}=570$.

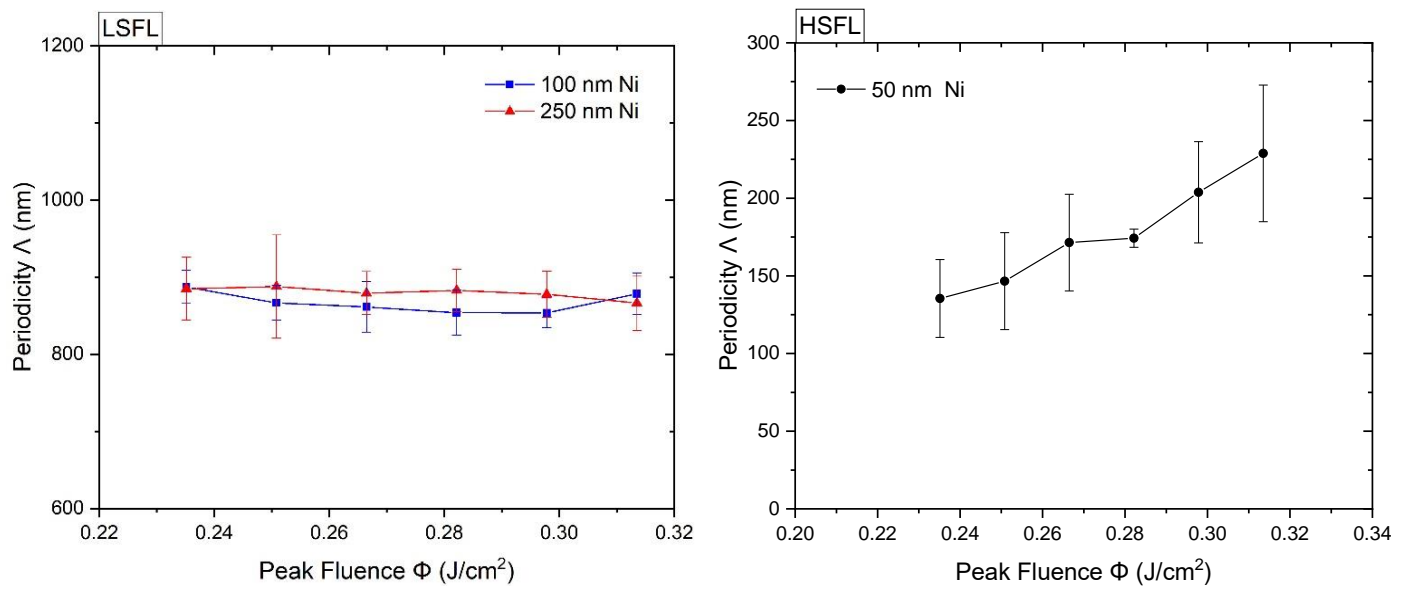


Figure 14
Graphs of periodicity as a function of laser fluence for $N_{eff}=114$.

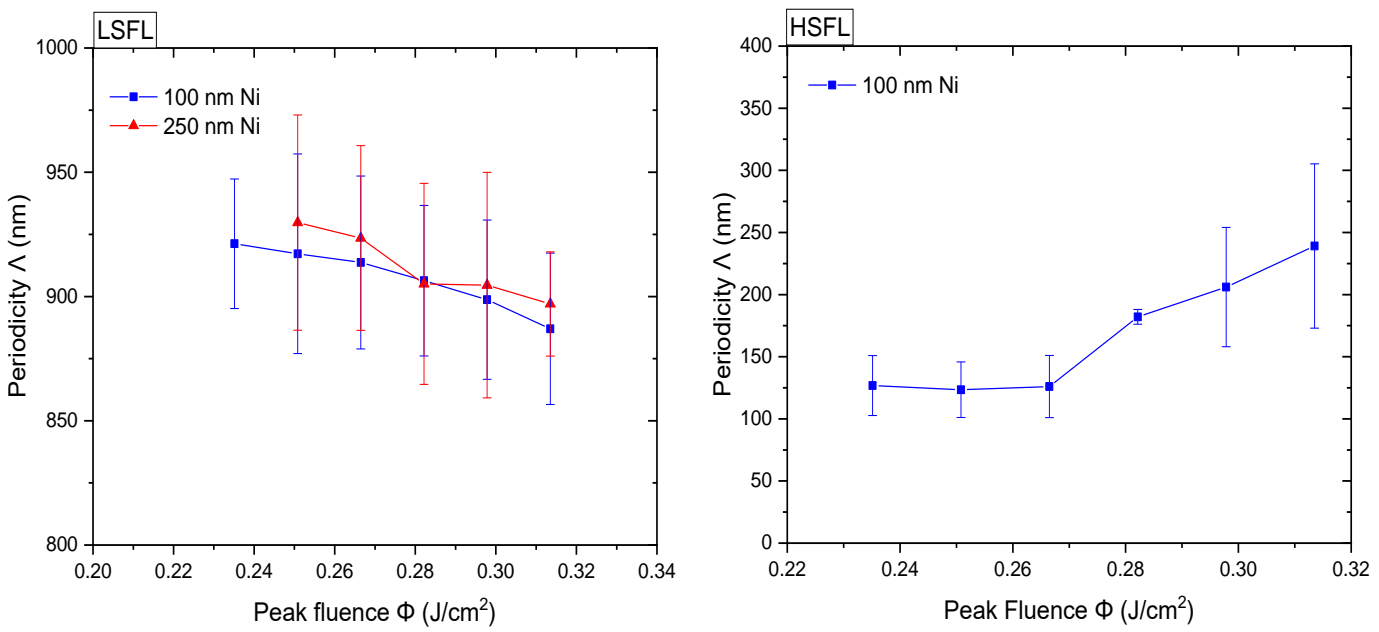


Figure 15
Graphs of periodicity as a function of laser fluence for $N_{\text{eff}} = 57$.

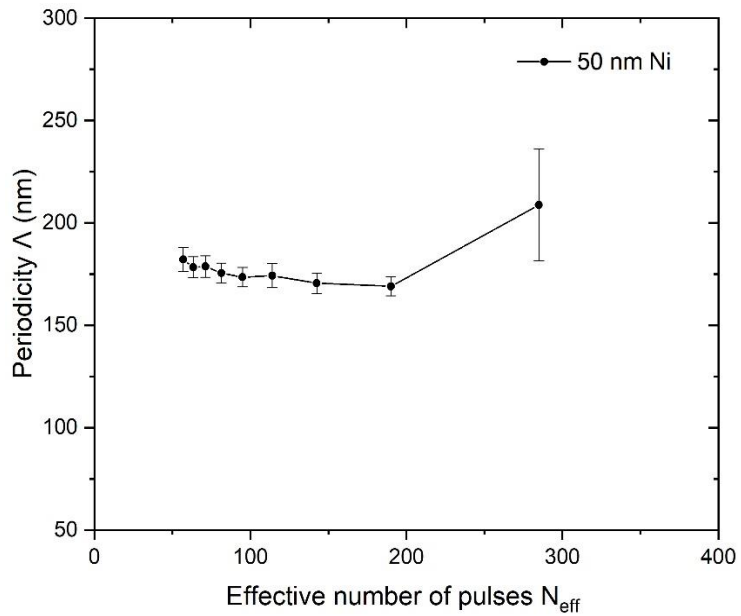


Figure 16
Graphs of HSFL periodicity as a function of effective number of fluences for $\Phi = 0.282 \text{ J}/\text{cm}^2$

The data from the graphs above, indicate certain behaviors of the structures on the Ni films. At first, it must be noted that the thinnest Ni film, 50 nm, features mainly HSFL structures that are oriented parallel to the laser beam's polarization and have a periodicity of approximately 100-200 nm. On the contrary, the thicker Ni films, 100 & 250 nm, present very different periodic structures as they are LSFL and their periodicity is close to 900-1000 nm, which is approximately equal to the laser's wavelength.

More specifically, for high number of pulses, the structures that we can see in this parametric study belong to the 50 & 100 nm Ni films. These LIPSS are LSFL and they have a periodicity that increases as the film gets thicker (*Figure 13*). As the effective number of pulses increases, the graphs of $\Lambda\text{-}\Phi$, in *Figure 14*, show the most common case, in which LSFL structures are present in 100 & 250 nm Ni films and HSFL structures are present in the 50 nm Ni film. Also, it is clear that the periodicity of the HSFL structures, on 50 nm Ni film, increases as the energy fluence increases, which is an indicator of the multivariance of the periodic structures on the thinnest Ni film. In other words, the form and periodicity of the structures on the thinnest film, are changing much more frequently than the structures on the thicker films, which is caused from the different mechanisms that lead to the formation of LIPSS in these two cases.

Moving on to *Figure 15*, we can see that there are no LIPSS on the 50 nm Ni film for a low number of pulses. On the other hand, the films of 100 & 250 nm Ni feature LSFL structures on their surfaces, which have periodicities that are pretty much constant in relation to the energy fluence. Furthermore, the 100 nm Ni film features both LSFL and HSFL structures, for this low pulse number. This behavior resembles the structures of 50 nm Ni, for bigger pulse numbers, as the periodicity of the LSFL structures in 100 nm Ni increases according to the energy fluence.

Lastly, *Figure 16* shows the dependence of the HSFL periodicity, of 50 nm Ni, on the different values of energy fluence. As it is clear, there is no particular dependence as the value of periodicity remains almost constant (at 100-200 nm) for the whole energy range.

- $\lambda=513\text{ nm}$

The irradiation of the same Ni samples, as before, using the same technique but radiation in the visible spectrum ($\lambda=513\text{ nm}$), provides data that show different morphologies and periodicities. A basic difference that was noticed during the transition from the use of IR beam to the VIS beam, was the very narrow energy range that was used. LIPSS appeared only in a short laser power range, making it difficult for the realization of a comparative study of same laser parameters but different films.

After each sample was studied thoroughly enough, so that the energy range, in which LIPSS were fabricated, was established, the parameters of the comparative study were decided. More specifically, the laser parameters that were used are the following:

Laser power range: $P = 0.1 - 1.0\text{ mW}$, with a step of 0.1 mW

$$\rightarrow \Phi = 0.036 - 0.365 \frac{\text{J}}{\text{cm}^2}$$

Scanning velocity: $v = 0.2 - 1.0 \frac{\text{mm}}{\text{s}}$, with a step of $0.2 \frac{\text{mm}}{\text{s}}$

\rightarrow Effective number of pulses: $N_{eff} = 26 - 132$

For the calculation of the energy fluence above, the spot size of the VIS beam was considered to be the average of the two values that were extracted from the damage threshold studies:

$$w_{0,vis} = (13.2 \pm 0.2) \mu\text{m}$$

Moving on, the SEM images taken from the lines of the parametric study, confirmed the fact that the Ni samples had a very narrow range of energy that could fabricate LIPSS, for the VIS beam. As a result, most of the lines that were fabricated, were partly or completely ablated.

Generally, the 50 nm film of Ni presented mainly lines that consisted of HSFL structures and more rarely lines that consisted of HSFL and LSFL structures, at the same time. The 100 nm Ni film was mainly consisted of LSFL structures that looked like “horizontal” nanowires. Lastly, the sample of 250 nm Ni was fabricated in a very similar way to the 100 nm Ni sample, as LSFL nanowires-like structures were created in its surface. Representative images of these structures are depicted in *Figure 17*.

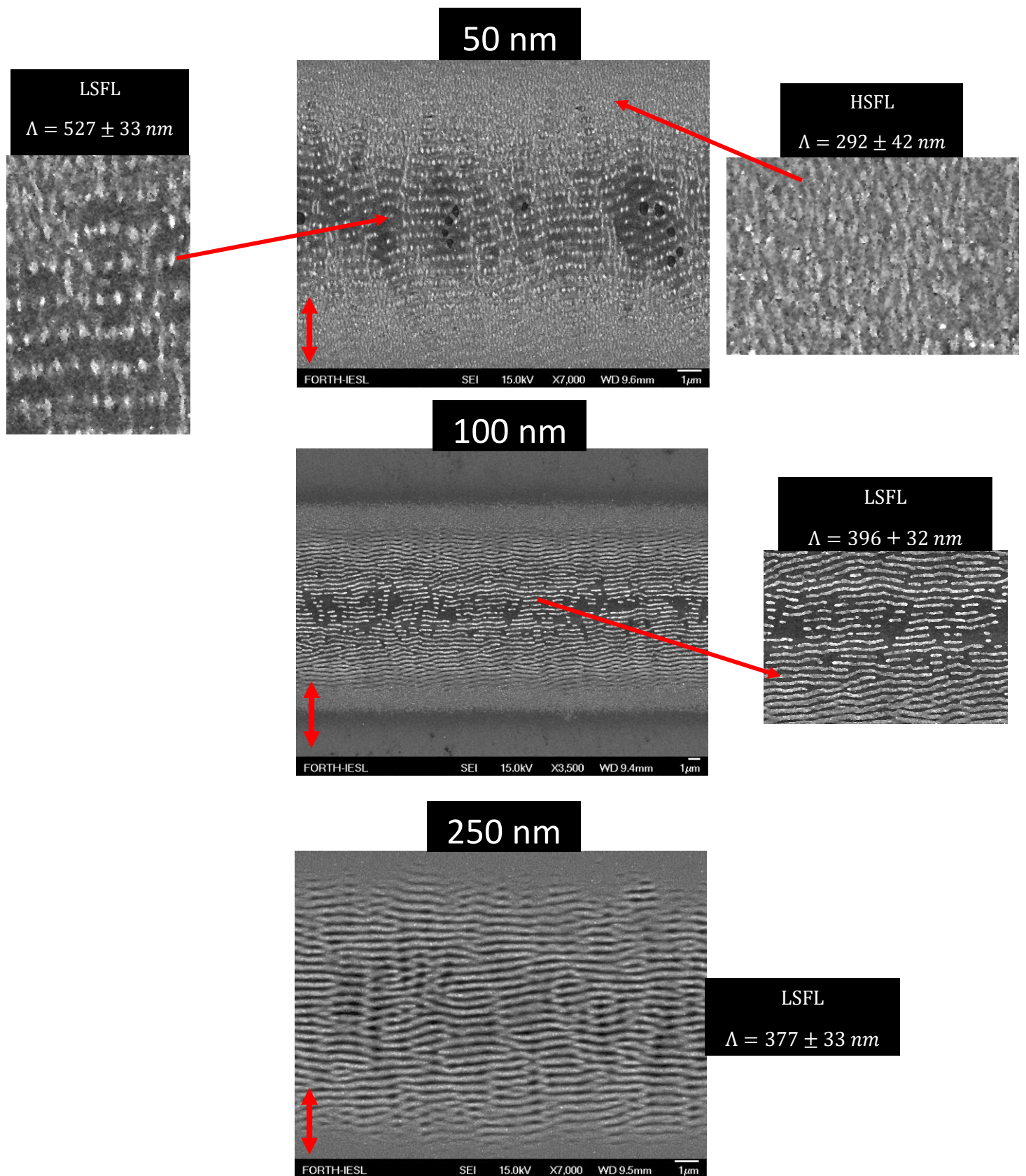


Figure 17

Images from SEM of 50, 100 & 250 nm Ni samples.

All the lines were created using the same laser energy fluence (0.219 J/cm^2) and effective number of pulses (66).

The graphs that show how periodicity of LIPSS changes according to the laser fluence and the effective number of pulses, appear in the figures below:

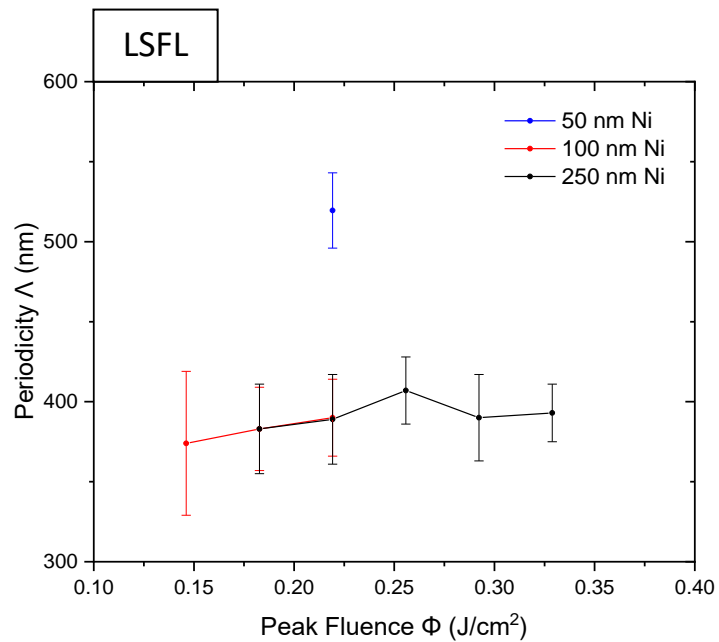


Figure 18
Graph of periodicity as a function of laser fluence, for $N_{\text{eff}} = 132$

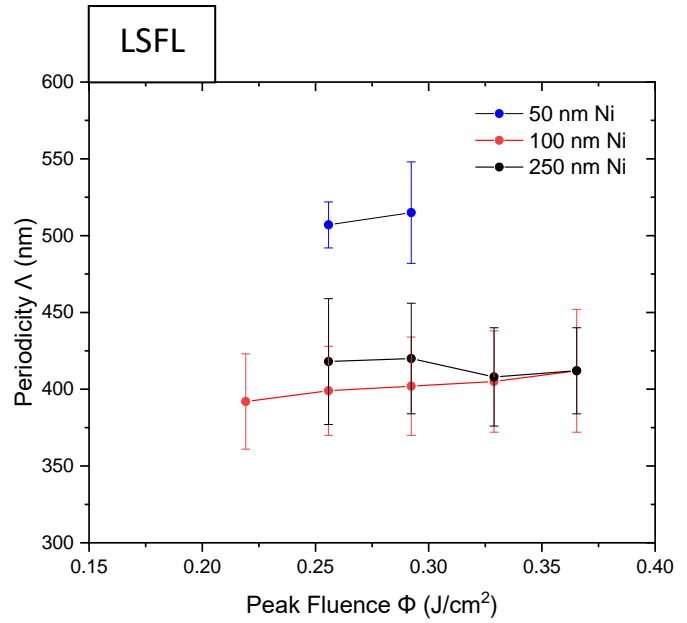
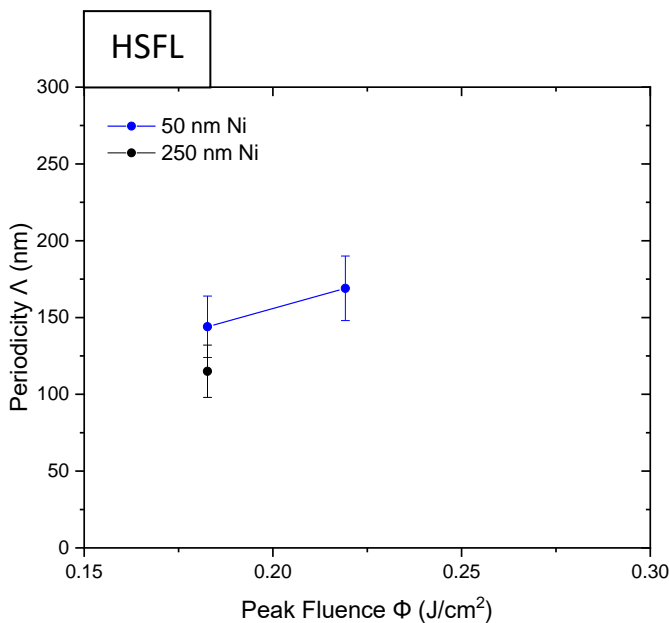


Figure 19
Graph of periodicity as a function of laser fluence, for $N_{\text{eff}} = 26$

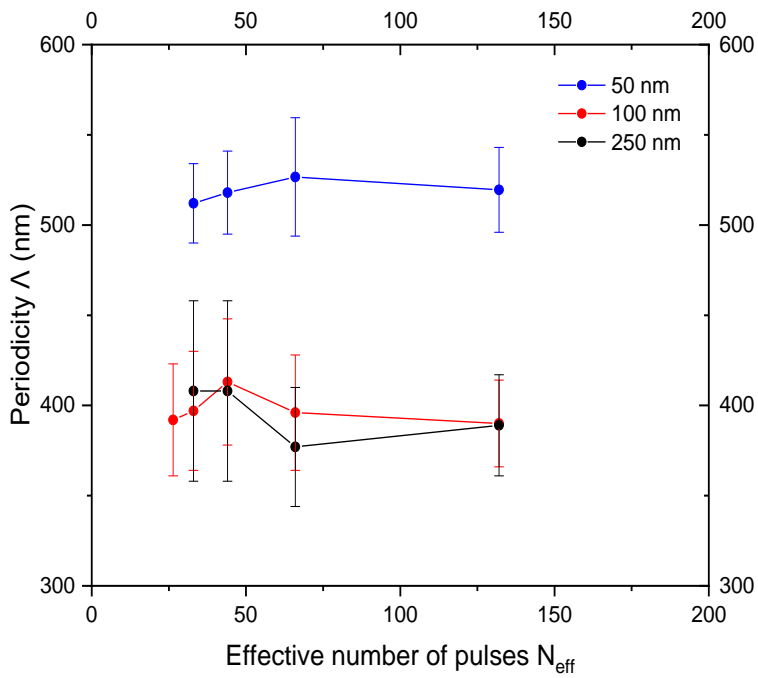


Figure 20
Graph of LSFL periodicity as a function of N_{eff} , for $\Phi = 0.219 \text{ J/cm}^2$

Based on the data from the graphs above, we can conclude some main observations. In *Figure 18*, the periodicity of LSFL structures of the Ni films is depicted as a function of energy fluence, while the number of pulses is constant. This graph refers to the largest number of pulses that is used in this parametric study and it is clear that the majority of the structures that can be seen, belong to the samples of 100 & 250 nm Ni, which are the thickest films of Ni. The periodicity of these LSFL structures is almost constant, for the different values of energy fluence, at 400-500 nm, which is a value very close to the wavelength of the radiation used (513 nm).

Moving on to lower values of number of pulses, the periodicity of LIPSS that are observed can be represented through *Figure 19*. Specifically, the sample of 50 nm Ni was consisted mainly of HSFL structures combined with LSFL structures in some cases. The HSFL structures had periodicities almost equal to the half of the laser's wavelength while the LSFL structures had periodicities almost equal to the laser's wavelength. Once more, we can see that the periodicity of the LSFL structures on 100 & 250 nm Ni films, are constant as a function of laser energy fluence and have a value close to that of the laser's wavelength. This can be noted also through *Figure 20*, in which we can see that the periodicity of the LSFL structures is constant as the value of the number of pulses changes.

4.1.2 Comparative study of Cr films

4.1.2.1 Calculation of damage threshold fluence of Cr films

Similar with the damage threshold studies of Ni films, the Cr films were irradiated with a range of single shot pulses that varied in laser power. Again, we used both of the laser radiations: 513 nm and 1026 nm beam, in order to obtain the damage threshold fluence of Cr in both radiations. The Cr films that were used in this study are: 10, 40, 100, 250 nm.

- $\lambda=1026 \text{ nm}$

The experimental procedure that was described previously in the Ni damage threshold fluence calculation, is implemented in the same way only with parameters that are adapted to the surface modification properties of Cr. The data that are produced are presented in *Table 4*:

Cr film thickness (nm)	Damage threshold fluence Φ (J/cm^2)	$\delta\Phi$ (J/cm^2)	Spot size w_0 (μm)	δw_0 (μm)
10	0.739	0.028	28.978	2.204
40	0.302	0.021	28.567	4.054
100	0.185	0.012	29.184	3.846
250	0.175	0.012	26.342	3.572

Table 4

Therefore, the average value of the spot size of the beam in IR is:

$$w_{0,IR} = (28.268 \pm 1.134) \mu\text{m}$$

- $\lambda=513$ nm

Similarly, the results that came from the data of the damage threshold study of Cr, using the 513 nm beam, are:

Cr film thickness (nm)	Damage threshold fluence Φ (J/cm ²)	$\delta\Phi$ (J/cm ²)	Spot size w_0 (μm)	δw_0 (μm)
10	0.171	0.014	10.817	1.710
40	0.147	0.001	13.601	0.184
100	0.118	0.001	14.560	0.343
250	0.133	0.001	14.866	0.101

And the estimated average value of the spot size in 513 nm radiation is:

$$w_{0,VIS} = (13.460 \pm 1.596) \mu\text{m}$$

The damage threshold energy fluence of the different thicknesses of Cr films are depicted in the graph below:

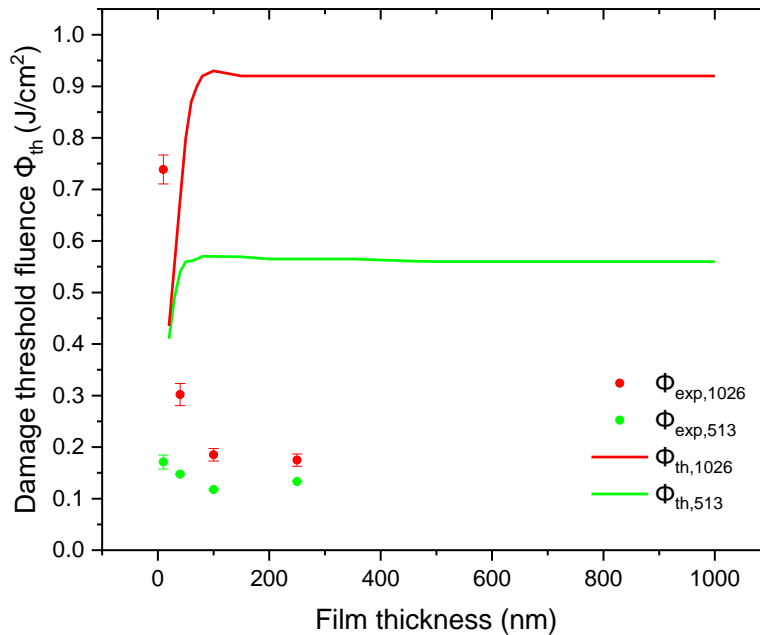


Figure 21

Experimental and theoretical graph of damage threshold fluence of Cr as a function of film thickness.

The graph above shows that the experimental data of Cr are not consistent with the theoretical curve that is depicted in the lower part of the graph. Instead of an increasing trend, the damage threshold fluence presents a decreasing trend, as a function of film's thickness. However, the experimental data that are obtained from the samples of 100 & 250 nm Cr, are placed in a damage threshold fluence plateau, which means that there is an experimental and theoretical agreement in the thickest films (> 100 nm).

This unexpected behavior may be caused from the quality of the metal film's deposition, for the samples of 10 & 40 nm Cr. Nevertheless, these data can not exclude any conclusion for the damage threshold of Cr thin films.

4.1.2.2 Parametric study of different thicknesses of Cr films

In this study, all 4 different thicknesses of Cr films on SiO₂, also used in previous study, were irradiated with 1026 nm radiation, forming lines on the samples' surface. Similar to the Ni parametric studies, the parameters that varied were: laser power and scanning velocity that correspond to energy fluence and effective number of pulses, respectively.

More analytically, the actual parameters that were used for this study were:

Laser power: 2.4 – 4.0 mW with a step of 0.4 mW

\rightarrow *Laser fluence: 0.193 – 0.313 $\frac{J}{cm^2}$ with a step of 0.03 J/cm²*

Scanning velocity: 0.2 – 1.0 $\frac{mm}{s}$ with a step of 0.2 mm/s

\rightarrow *Effective number of pulses: 57 – 285*

In the following paragraphs, the SEM images of the most representative morphologies of the LIPSS fabricated on all of the Cr samples, are going to be presented.

The irradiation of the different thicknesses of Cr films: 10, 40, 100 & 250 nm, with the same fluence and number of pulses, produces a variety of different LIPSS on the samples' surface. As it is clear in *Figure 22*, the film of 250 nm Cr appears to have LSFL nanowires ($\Lambda = 862$ nm) while the 100 nm film has also LSFL structures ($\Lambda = 442$ nm) that, however, resemble "broken" nanowires. Moving on to the thinner films, the 40 nm Cr film's surface also presents LSFL structures ($\Lambda = 305$ nm) that are even smaller and more scattered than the thicker films. At last, the 10 nm Cr film is consisted of some non-specific structures, therefore their periodicity cannot be calculated properly. The only LIPSS that were observed, on the sample of 10 nm Cr, are LSFL structures that appear only for a small number of pulses.

More specifically, apart from the nanowires structures, the sample of 250 nm Cr presents ablated lines in a large percentage. However, these results are not very reliable due to the quality of the film's deposition. *Figure 23* shows two images of fabricated lines in 250 nm Cr, that are irradiated with the highest and lowest value of energy fluence, using the same number of pulses. As it is clear, this behavior is not at all normal, because the highest the energy fluence is, the more intense the ablation is. This is not the case for these images, as we can see that the lowest value of fluence created ablated lines, and not the

other way. Furthermore, another indication of the film's questionable quality is the cracks that appear in *Figure 23*, at low fluence.

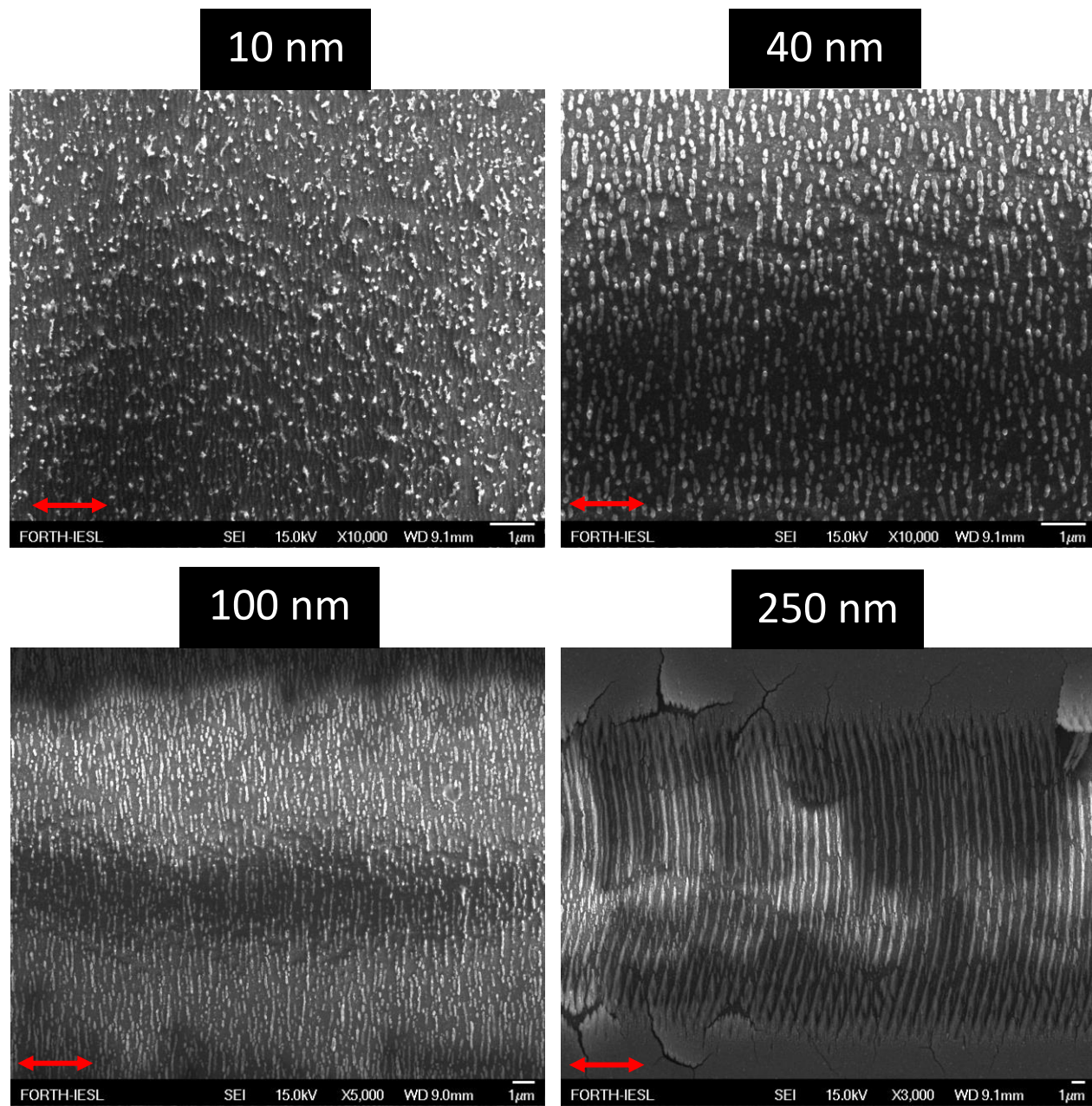


Figure 22

SEM images of LIPSS fabricated in different thicknesses of Cr films by irradiation with 1026 nm beam.
Laser fluence: 0.253 J/cm^2 and $N_{\text{eff}}=95$

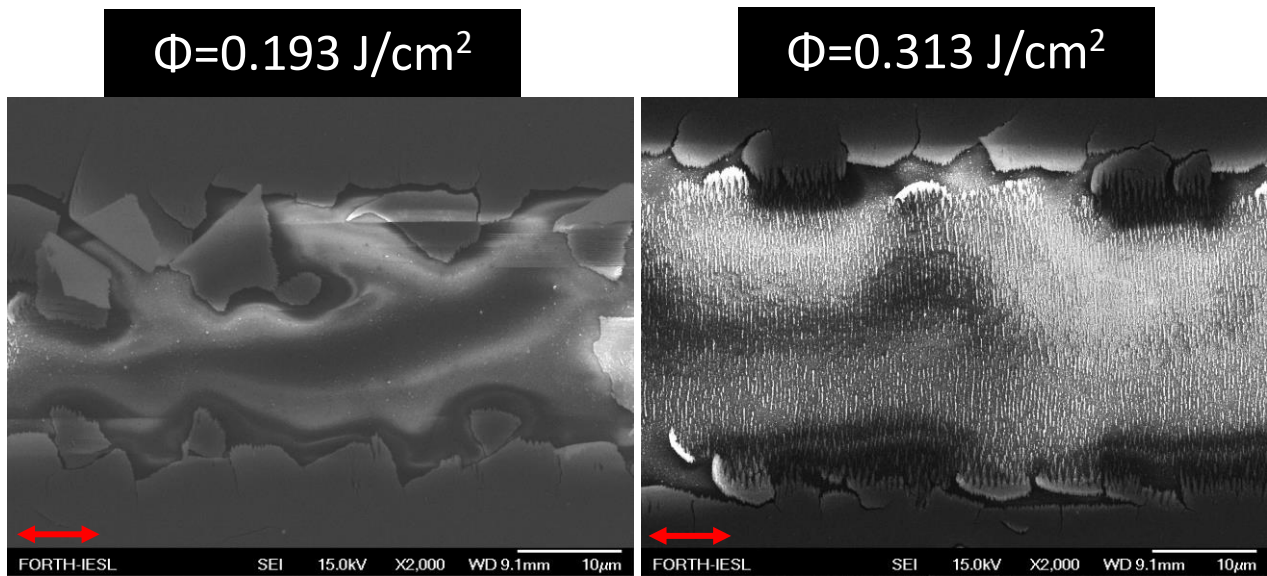


Figure 23

SEM images of the irradiated surface of 250 nm Cr film. On the image on the left, the fluence is low while on the right the fluence is high. The same number of pulses was irradiated in both cases.

Generally, the films of 40 and 100 nm Cr show the same kind of LSFL structures across all the data of different fluences and number of effective pulses that were used. Nevertheless, the 10 nm film of Cr presents some interesting SEM images. In the most part of this study, the SEM images presented unclear or no periodicities at all, for this sample. But there were certain images, whose morphologies were consisted of structures that are perpendicular to the laser polarization (*Figure 24*). These structures are more distinct in the lines that were fabricated with low number of pulses (*Figure 24c*).

The graphs that represent the structures' periodicity as a function of the laser fluence and the effective number of pulses, that were used in this comparative study, are depicted in *Figures 25-27*.

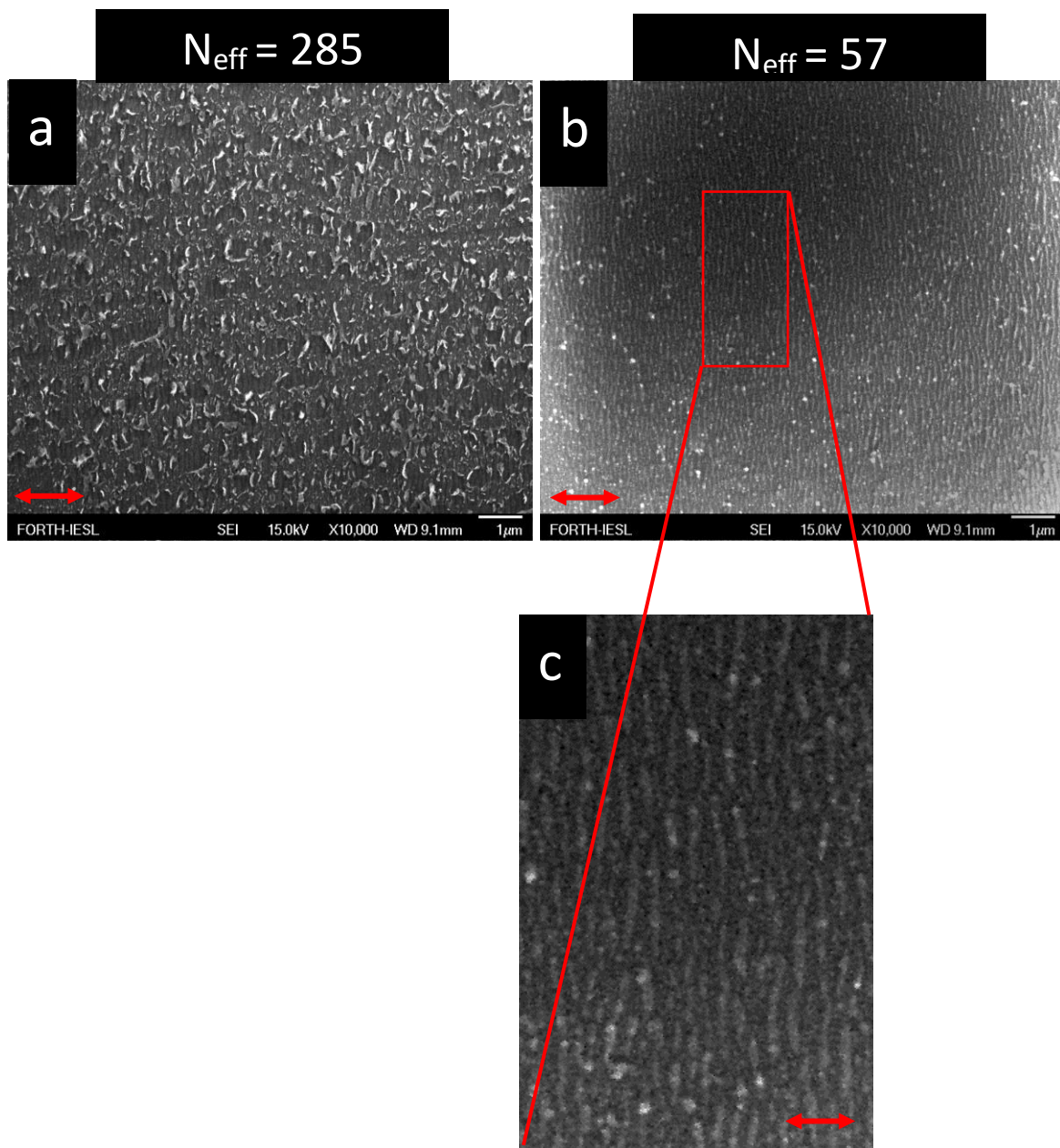


Figure 24

SEM images of the irradiated surface of 10 nm Cr film.

The same energy fluence was used in both cases.

- a. High number of pulses,
- b. Low number of pulses,

c. Zoomed image of the structures that are perpendicular to the laser polarization.

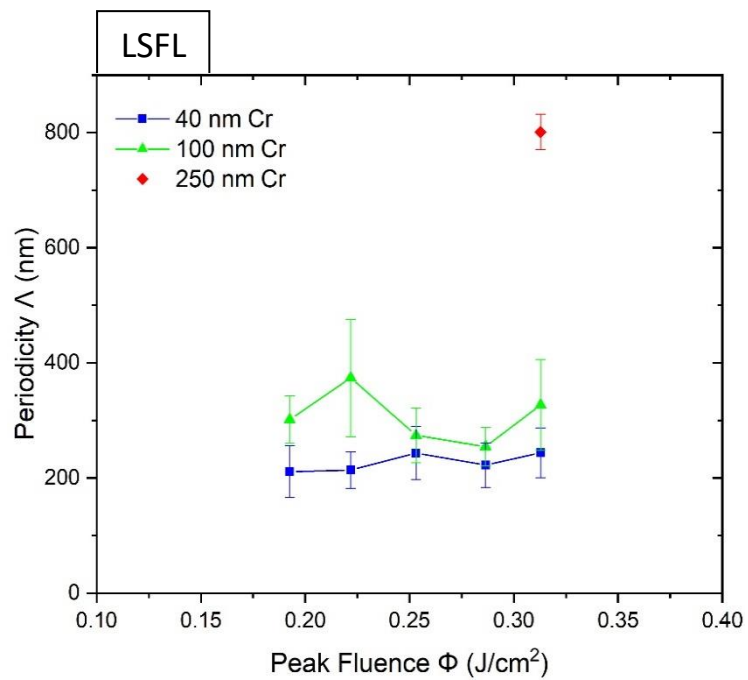


Figure 25

Graph of periodicity of structures on Cr thin films, as a function of laser fluence, for $N_{eff} = 285$

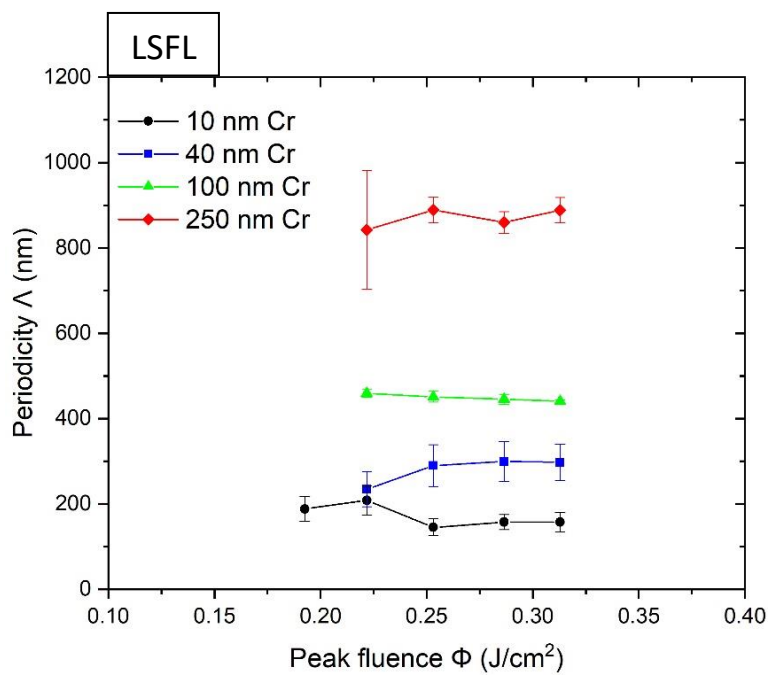


Figure 26

Graph of periodicity of structures on Cr thin films, as a function of laser fluence, for $N_{eff} = 57$

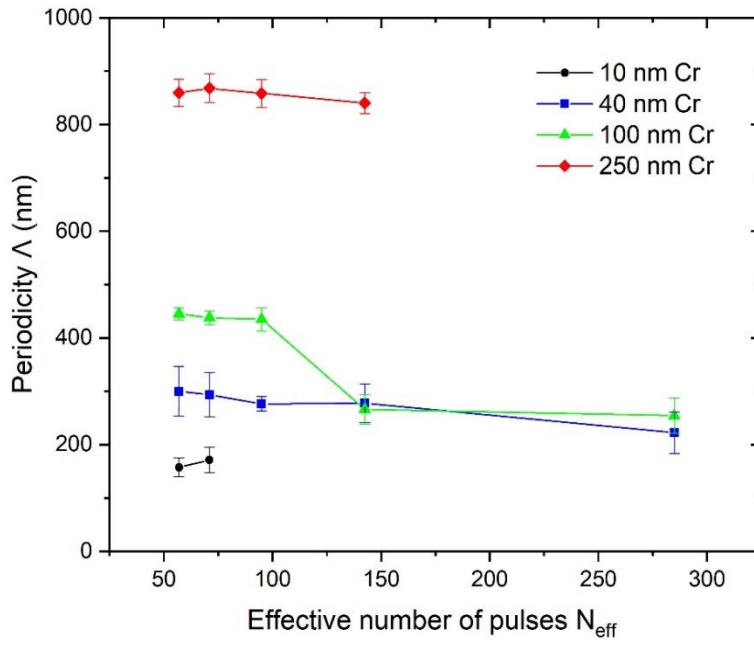


Figure 27

Graphs of periodicity of LSFL structures on Cr thin films, as a function of effective number of pulses, for $\Phi = 0.29 \text{ J/cm}^2$

Figures 25 and 26, show the periodicities of the LSFL structures that are featured on the surface of all 4 samples of Cr, for a constant number of pulses and a varying value of energy fluence. Specifically, Figure 25 consists of data that were taken using the largest value of pulses, from the range of this parametric study, and Figure 26 corresponds to the lowest value of pulses.

As we can see, using a high value of irradiated pulses, only the samples of 40 and 100 nm Cr, feature any LIPSS, as the sample of 10 nm Cr is not structured at all and the sample of 250 nm Cr features only some cracks, due to the bad quality of the film's deposition. On the other hand, the graph of low value of irradiated pulses, shows similar values of periodicity for the 40 and 100 nm Cr films, and also shows the presence of LSFL structures on both 10 and 250 nm Cr films. The LSFL structures of 250 nm appear for larger numbers of pulses, as this energy deposition does not crack the surface of the film.

When it comes to the film of 10 nm Cr, we can conclude that the LSFL structures appear only on low values of pulses, where possibly the Cr film is ablated and we can see the structures on top of the dielectric substrate. There is a high possibility that these LSFL structures are not actually LSFL, but they are HSFL structures on top of the fused silica substrate. This may provide a very important finding, as the normal value of LIPSS fabrication of fused silica is 10 times greater than the energy fluence value that was used

in this study. Therefore, this may lead to a new way of fabricating glass made of fused silica, using lower laser power.

Another important finding from this parametric study of Cr thin films, is that the periodicity of the LSFL structures, on all 4 samples, increases as the film thickness increases. This is also supported from the data of *Figure 27*.

4.2 Fabrication of nanowires on Cr thin films

4.2.1 Nanowires area on 400 nm Cr film

In the previous comparative study of thin film and bulk film metals, many morphologies presented the characteristics of nanowires, either vertical or horizontal. A previous study of nanowires fabrication on 100 nm Ni film, confirmed the potential of fabrication of a horizontal nanowires topology, using 513 nm radiation [5]. This study's initial aim was to explore the potential of fabrication of nanowires in a large area of a 400 nm Cr film. The results from this study can determine whether the morphology of nanowires can be fabricated in thicker films, providing a more sufficient grid polarizer.

The first step of this study was to find the appropriate parameters that are needed in order to create such a surface morphology. Parametric studies that were conducted using the two different radiations of the experimental setup, IR and VIS, indicated that the use of IR radiation could not result in nanowires fabrication. Thus, this study was realized through the use of IR radiation, 1026 nm, and the appropriate energy range, for the 400 nm Cr sample, was selected to be:

Laser power range: $P = 3.0 - 5.0 \text{ mW}$, with a step of 1.0 mW

$$\rightarrow \text{Laser energy fluence: } \Phi = (0.244 - 0.399) \frac{\text{J}}{\text{cm}^2}$$

The parametric studies were conducted via line formation and the scanning velocity that was used for this purpose was:

$$\text{Scanning velocity: } v = (0.1 - 1.0) \frac{\text{mm}}{\text{s}}, \text{ with a step of } 0.1 \frac{\text{mm}}{\text{s}}$$

$$\rightarrow \text{Effective number of pulses: } N_{\text{eff}} = 57 - 570$$

This parametric study resulted in many different conditions that can be used for the fabrication of nanowires, in the shape of a line. Among them, the line and the corresponding conditions that were distinguished are presented in *Figure 28*.

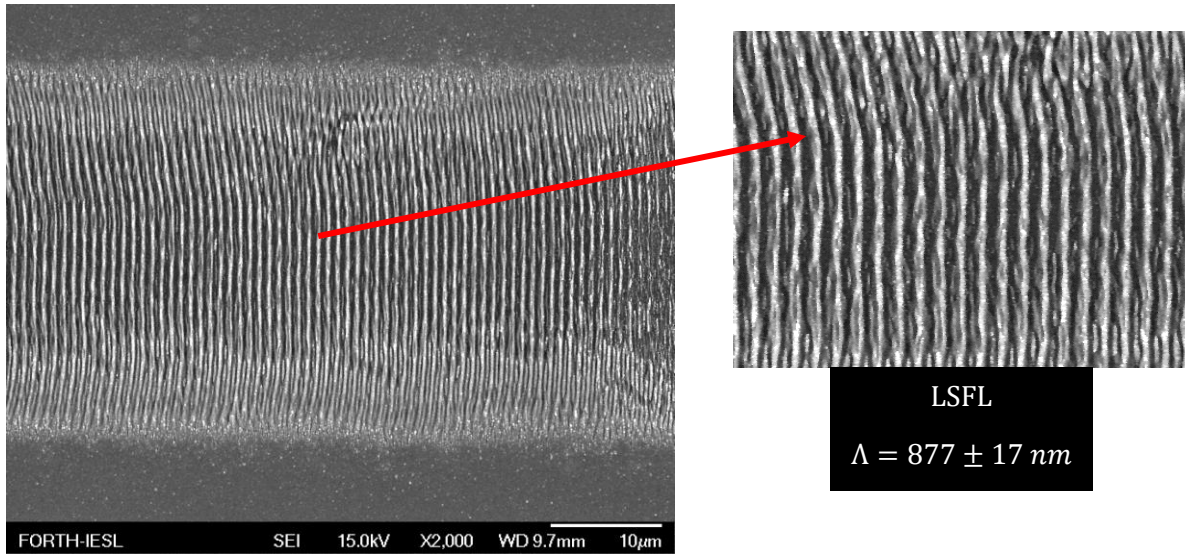


Figure 28

SEM images of the nanowires line that was fabricated using the optimum conditions:

$$\Phi = 0.324 \frac{\text{J}}{\text{cm}^2}, \quad N_{\text{eff}} = 71.25$$

Having configured the optimum conditions that are needed in order to fabricate nanowires on the surface of 400 nm Cr film, the next step is to simulate the same nanowires in a larger area (1 cm x 1 cm). As a trial, many different areas were fabricated, in smaller areas (200 μm x 200 μm), testing different parameters each time: scanning line speed, distance between lines (Y step).

The effective number of pulses that falls in the area of the beam's spot size, during the scanning of an area, is given by the following relation:

$$N_{\text{eff,area}} = \frac{\pi w_0^2 f}{v Y},$$

where:

f: the repetition rate of the laser pulse,

v: line scanning velocity,

w₀: the beam's spot size,

Y: the distance left between the scanned lines, previously mentioned as Hatch.

The parameters used for this study were various. The energy fluence (0.324 J/cm²) that was used is the same but the scanning velocity was not selected to be the same. In order to create the most uniform and consistent area, the scanning velocity needed to be twice

the value of the optimum line scanning velocity: $v = 1.6 \frac{mm}{s}$, and the hatch needed to be half the value of the line's width. In *Figure 28*, the line's width is approximately 30 μm , while the nanowires morphology is limited to only 21 μm of this length.

However, the multiple area tests resulted to the selection of the following optimum area conditions:

$$Y = 25 \mu m, v = 0.8 \frac{mm}{s}$$

$$\rightarrow N_{eff} = 128$$

$$\& \Phi = 0.324 \frac{J}{cm^2},$$

dimensions: 1 cm x 1 cm

The resulted morphology of the area is depicted in *Figure 29*. The nanowires morphology that was created appears to have very well oriented wires that are parallel to each other ($\Lambda=857 nm$). However, the LSFL structures with periodicity $\Lambda=430 nm$, that are in between the well oriented nanowires that were mentioned previously, show a very different morphology that does no quite resemble nanowires. These structures are fabricated because of the large Y value that was selected for the fabrication of the nanowires area.

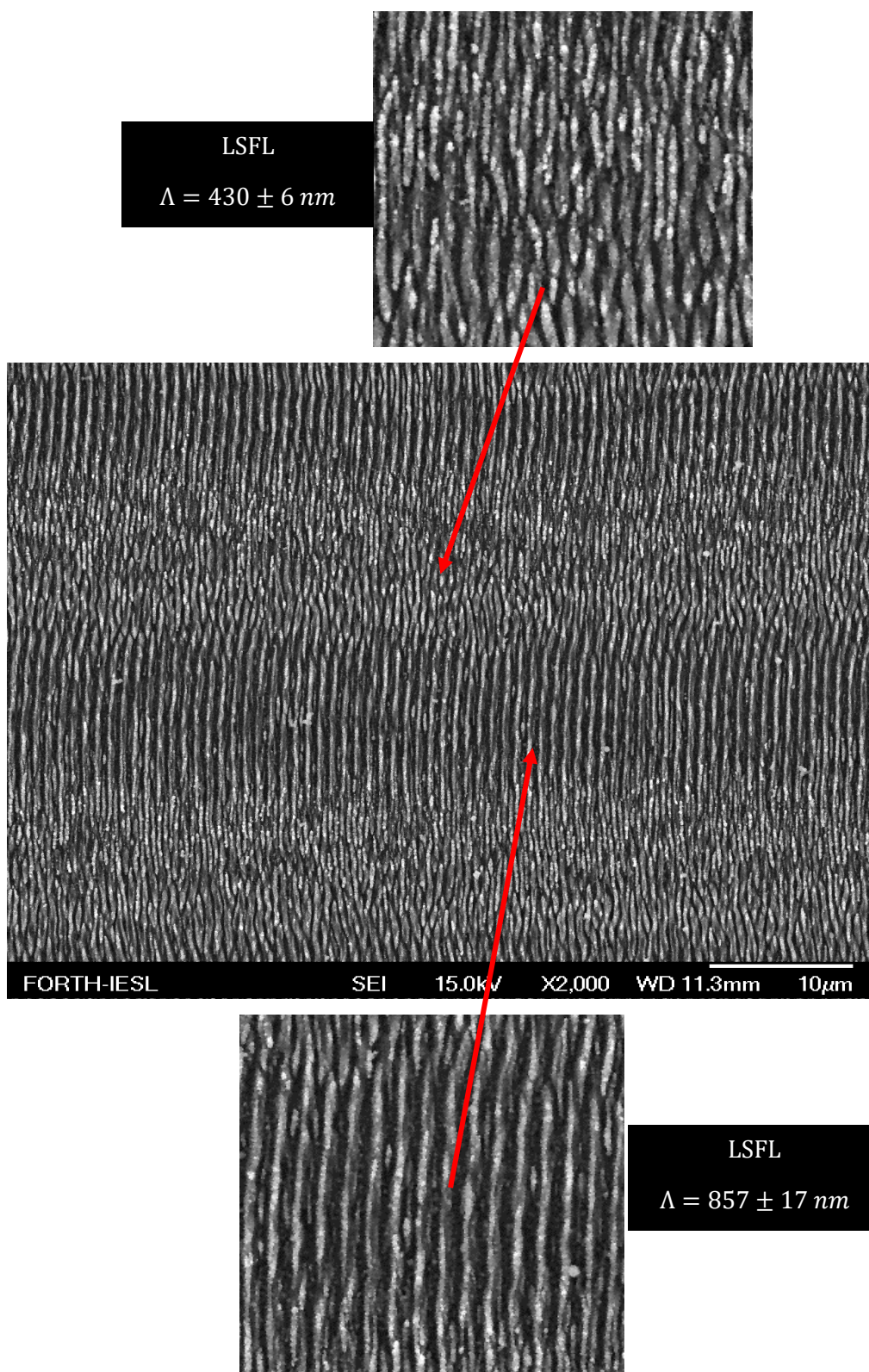


Figure 29

SEM image of a part of the 1 cm x 1 cm area that was fabricated with the optimum conditions described above, in 400 nm Cr film.

4.2.2 Nanowires area on 250 nm Cr film

This study was continued with the fabrication of nanowires also on the sample of 250 nm Cr on SiO₂. After following a detailed parametric study, for the selection of the most appropriate conditions that replicate this morphology, the final parameters that were used are:

$$Y = 15 \mu\text{m}, v = 2 \frac{\text{mm}}{\text{s}}, P = 4.03 \text{ mW}$$

$$\rightarrow N_{eff} = 85, \Phi = 0.316 \frac{\text{J}}{\text{cm}^2}$$

dimensions: 0.5 cm x 0.5 cm

The final image of the fabricated area is given in *Figure 30*, below:

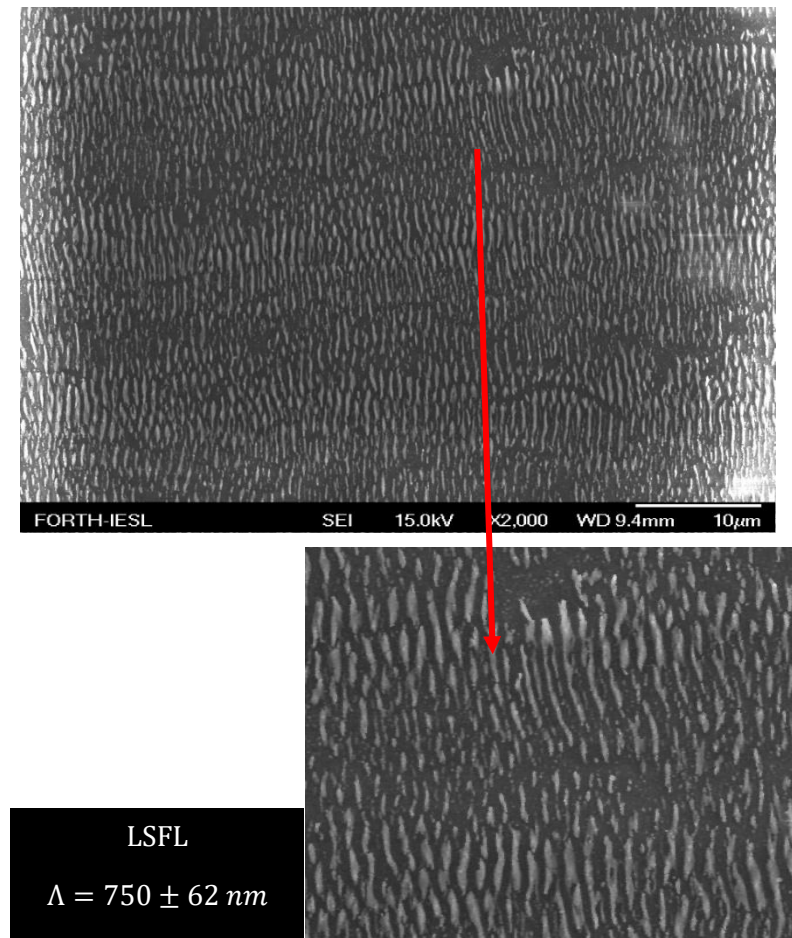


Figure 30

SEM image of a part of the nanowires area that was fabricated with the optimum conditions described above, in 250 nm Cr film.

In this area of nanowires that was fabricated, we can see that the nanowires morphology is not that homogeneous and parallel as we hoped that it would be. The transition from the fabrication of a line to the fabrication of an area, reveals many problems when it comes to the homogeneity of the structures in the area. However, the quality of both nanowires surfaces, on 250 and 400 nm Cr, when it comes to their use in Wire Grid Polarizers, was not studied as there was no time for optical measurement of each surface through spectrum analysis.

4.2.3 Nanoislands area on 250 nm Cr film

Another interesting approach was the fabrication of circular “islands” on the surface of the same sample, but with the use of a circularly polarized laser beam, in 1026 nm. The parameters that were selected, in this case, are:

$$Y = 7 \mu m, v = 1.8 \frac{mm}{s}, P = 3.01 mW$$

$$\rightarrow N_{eff} = 202, \Phi = 0.236 \frac{J}{cm^2}$$

dimensions: 0.5 cm x 0.5 cm

The SEM image of the line that was used as the optimum conditions for the fabrication of the area, in the 250 nm Cr film, is given below:

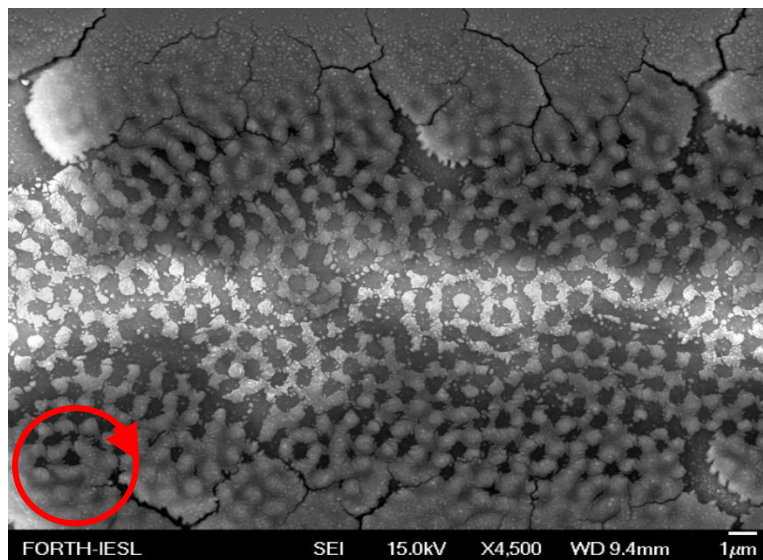


Figure 31

SEM image of the line with the optimum conditions for the fabrication of a circular “island” area, in 250 nm Cr film.

In the image above, the circular nanoislands that were fabricated with the circular polarization of the beam, present an interesting morphology for use in cell cultures, as it is consisted of blank spaces in between the islands, in which cells can fit in during their growth on the surface.

4.2.4 Cell adhesion on nanowires and nanoisland surfaces

The results from the study of cell cultures that were grown on the surfaces of 250 & 400 nm Cr with nanowires, on 250 nm Cr with nanoislands and also on the flat surface of Cr, are given below:

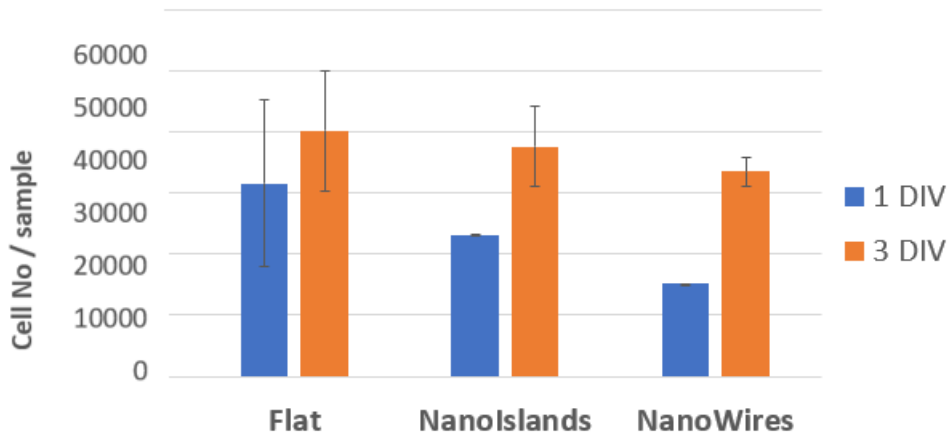


Figure 32
Chart of the cell number per different morphology.

The chart above shows the cell number in every different surface sample for two different time frames of cell growth: 1 day (blue) and 3 days (orange). It is clear that the number of cells that grew in the nanostructured surfaces is smaller than the flat surface, in both cases of nanoislands and nanowires. This is because of the certain form, geometry and size of the cells' body, which determines how many cells can actually multiply and grow on each surface. Therefore, the nanostructured surfaces present some limitations to the cell growth compared to the flat surface, that has the largest number of cell at the end of each time frame.

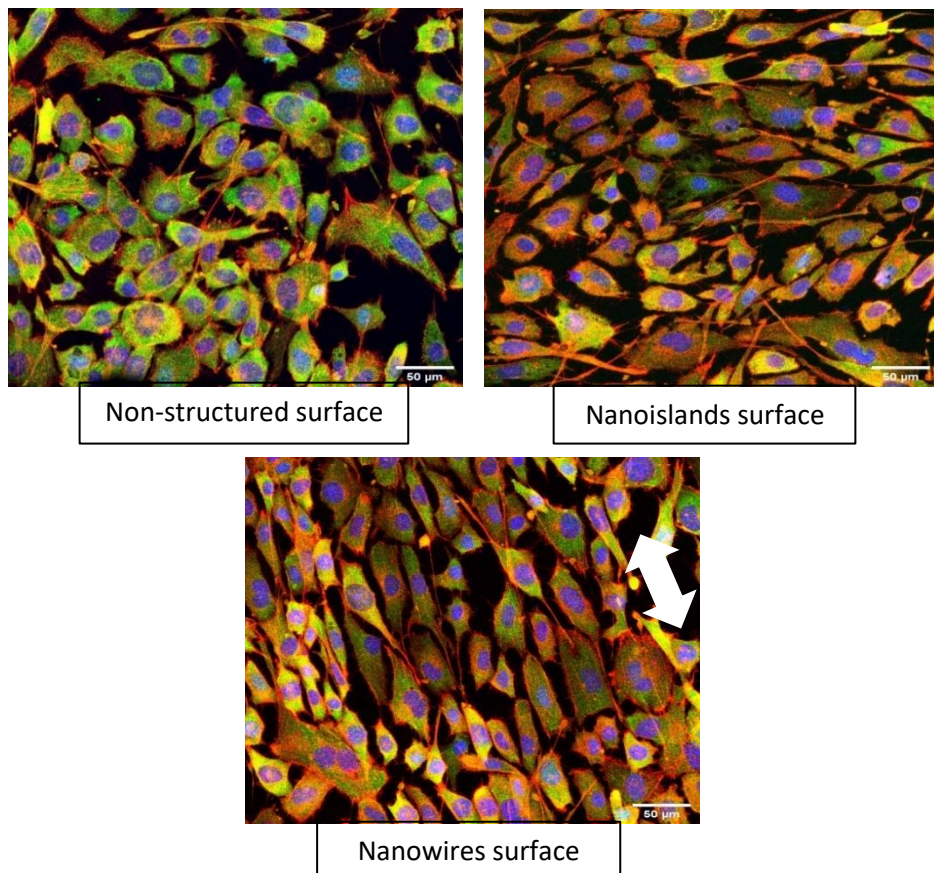


Figure 33

Images taken from the confocal microscope that show the cell cultures that grew on top of the different surface morphologies.

Figure 33 shows the cells that grew on the surface of each different morphology, in a scale of 50 μm , as the scale bar shows on the lower right corner of each image. It must be noted that the red color in each image is corresponding to a pigment that is concentrated on the cytoskeleton and therefore shows the cell morphology and orientation. The blue pigment indicates the cell nucleus, thus the cell proliferation and the green pigment shows the points of cell adhesion.

The non-structured surface features a number of cells that are not oriented in any way. Similarly, the nanoislands surface presents the same number of cells, approximately, and there is also no certain orientation of the cells' growth. However, the nanowires surface presents a cell culture that has orientation parallel to the nanowires orientation, which makes clear that the cells grew according to the morphology of the nanowires. Also, the shape of the cells is long and narrow compared to the previous cell morphologies on the nanowires and non-structured surfaces. Therefore, the nanowires surface is suitable to be used for many applications of cell growth and tissue generation.

5. Conclusion

At last, there are many conclusions that can be extracted from the experimental analysis and the results that were presented in this thesis. The most important finding of all is the definition of the relation between the periodicity of LIPSS on thin film metals and the thickness of the metal film, where we realized that as the film gets thinner, the periodicities of LIPSS get smaller. This is very important for the fabrication of LIPSS that have even smaller periodicity than 100 nm and therefore can be used in a variety of metasurfaces and other applications as well.

Secondly, the implementation of the parametric studies' data for the purpose of the fabrication of a surface morphology of nanowires provided many different types of data. On the one hand, the nanowires morphology was not as homogenous and periodic as the morphology of a Wire Grid Polarizer. On the other hand, this morphology provided very interesting data for the cell adhesion application. This way, the nanowires can be fabricated in a large surface and get used in a variety of biological applications, that involve cell and tissue growth on specific regions of surfaces.

Bibliography

1. Birnbaum, M. (n.d.). Semiconductor Surface Damage Produced by Ruby Lasers. *Journal of Applied Physics*, pp. 3688-3689.
2. Bonse, J. (2020). Quo Vadis LIPSS?- Recent and Future Trends on Laser-Induced Periodic Surface Structures. *Nanomaterials*.
3. Camilo Florian Baron, A. M. (2018). Biomimetic surface structures in steel fabricated with femtosecond laser pulses: influence of laser rescanning on morphology and wettability. *Beilstein J. Nanotechnology*.
4. E. Stratakis, J. B. (2020). Laser engineering of biomimetic surfaces. *Materials Science & Engineering*.
5. Evangelos Skoulas, A. C. (2020, November 11). Laser induced periodic surface structures as polarizing optical elements. *Applied Surface Science*.
6. Skoulas, E. (2020). Surface structuring of bulk and thin film materials with polarized ultrashort laser pulses. *PhD*.
7. Emmony, D. C. (1983). Laser mirror damage in germanium at 10.6 μm . *Appl. Phys. Lett.*
8. Sipe, J. E. (1983). Laser-induced periodic surface structure I. Theory. *Phys. Rev. B*.
9. Sipe, J. E. (1989). Laser Induced Periodic Surface Structure: An Experimental And Theoretical Review. *Ursu, I.*
10. Bai X. P., Z. H. (2011). Fabrication of engineered heart tissue grafts from alginate/collagen barium composite microbeads. *Biomed. Mater.*
11. Liu, J. M. (1982). Simple technique for measurements of pulsed Gaussian-beam spot sizes. *Opt. Lett.* 7, p. 196.

Acknowledgements

First of all, I would like to thank Mr. Stratakis Emmanuel, for his consistent support and guidance in every matter of my thesis. He truly provided me with many tools and aspirations for my future in experimental physics.

Also, I would like to thank Skoulas Evangelos, who was my everyday assistance in many aspects of my thesis, both experimentally and theoretically. However, his most important contribution was the trust he showed me in every problem that I had to encounter.

Last but not least, I want to thank Mr. Tsibidis George, who helped me in every theoretical question that was raised, during the time of my thesis. I also want to mention every member of the lab that was there to help me, whenever I came upon a technical issue.

Lastly, I want to thank Mrs. Aleka Manoussaki, for the never-ending hours she spent with me in the SEM clean room, taking pictures for my thesis, while she provided me with her wise advices.